

## Accepted Manuscript

Design, synthesis, and biological evaluation of 2,4-dihydropyrano[2,3-c]pyrazole derivatives as autotaxin inhibitors

Tatu Pantsar, Prosanta Singha, Tapio J. Nevalainen, Igor Koshevoy, Jukka Leppänen, Antti Poso, Juha M.A. Niskanen, Sanna Pasonen-Seppänen, Juha R. Savinainen, Tuomo Laitinen, Jarmo T. Laitinen



PII: S0928-0987(17)30401-3

DOI: doi: [10.1016/j.ejps.2017.07.002](https://doi.org/10.1016/j.ejps.2017.07.002)

Reference: PHASCI 4125

To appear in: *European Journal of Pharmaceutical Sciences*

Received date: 24 May 2017

Revised date: 28 June 2017

Accepted date: 3 July 2017

Please cite this article as: Tatu Pantsar, Prosanta Singha, Tapio J. Nevalainen, Igor Koshevoy, Jukka Leppänen, Antti Poso, Juha M.A. Niskanen, Sanna Pasonen-Seppänen, Juha R. Savinainen, Tuomo Laitinen, Jarmo T. Laitinen, Design, synthesis, and biological evaluation of 2,4-dihydropyrano[2,3-c]pyrazole derivatives as autotaxin inhibitors, *European Journal of Pharmaceutical Sciences* (2017), doi: [10.1016/j.ejps.2017.07.002](https://doi.org/10.1016/j.ejps.2017.07.002)

This is a PDF file of an unedited manuscript that has been accepted for publication. As a service to our customers we are providing this early version of the manuscript. The manuscript will undergo copyediting, typesetting, and review of the resulting proof before it is published in its final form. Please note that during the production process errors may be discovered which could affect the content, and all legal disclaimers that apply to the journal pertain.

# Design, Synthesis, and Biological Evaluation of 2,4-dihydropyrano[2,3-*c*]pyrazole Derivatives as Autotaxin Inhibitors

Tatu Pantsar<sup>a,\*1</sup> tatu.pantsar@uef.fi, Prosanta Singha<sup>b,1</sup>, Tapio J. Nevalainen<sup>a</sup>, Igor Koshevoy<sup>c</sup>, Jukka Leppänen<sup>a</sup>, Antti Poso<sup>a,d</sup>, Juha M.A. Niskanen<sup>b</sup>, Sanna Pasonen-Seppänen<sup>b</sup>, Juha R. Savinainen<sup>b</sup>, Tuomo Laitinen<sup>a</sup>, Jarmo T. Laitinen<sup>b</sup>

<sup>a</sup>School of Pharmacy, Faculty of Health Sciences, University of Eastern Finland, PO Box 1627 FI-70211 Kuopio, Finland

<sup>b</sup>School of Medicine, Institute of Biomedicine, Faculty of Health Sciences, University of Eastern 5 Finland, 70211 Kuopio, Finland

<sup>c</sup>Department of Chemistry, University of Eastern Finland, P.O. Box 111, FIN-80101 Joensuu, Finland

<sup>d</sup>Department of Internal Medicine VIII, University Hospital Tuebingen, 72076 Tuebingen, Germany

\*Corresponding author at: School of Pharmacy, Faculty of Health Sciences, University of Eastern Finland, PO Box 1627, FI-70211 Kuopio, Finland.

## 1. Introduction

Autotaxin (ATX) (EC number: 3.1.4.39), encoded by the *ENPP2* gene, is a secreted glycoprotein and the only member of the ectonucleotide pyrophosphatase/phosphodiesterase family (ENPP) that has lysophospholipase D (lysoPLD) activity (Umezū-Goto et al., 2002). ATX hydrolyses lysophosphatidylcholine (LPC) to produce lysophosphatidic acid (LPA) and choline. LPA is a bioactive lipid, which binds and signals mainly through specific G-protein-coupled lysophosphatidic acid receptors 1 to 6 (LPA<sub>1-6</sub>) (Kihara et al., 2014). In human, ATX is ubiquitously expressed and is also present in blood (Aoki et al., 2002). For specific spatiotemporal signaling, ATX is recruited on the cell surface by activated  $\beta_3$ -integrins (Leblanc et al., 2014; Pamuklar et al., 2009). Upon binding via its somatomedin B-like (SMB) domains to integrins (Hausmann et al., 2011), ATX is tethered to plasma membrane, promoting thereby allocated LPA-signaling. The localized increase in LPA concentration results in specific biological response, as LPA stimulates cell migration, proliferation and survival (Moolenaar et al., 2004), induces platelet aggregation and chemotaxis (Jalink et al., 1993), smooth muscle contraction (Tokumura et al., 1994), neurite remodeling (Fukushima et al., 2002) and ion channel activity (Iftinca et al.,

---

<sup>1</sup> T.P. and P.S. contributed equally and are considered as co-first-authors.

2007). Therefore, ATX contributes to various physiological and pathophysiological processes, such as embryonic development (Moolenaar et al., 2013), wound healing (Lee et al., 2013), inflammation (Knowlden and Georas, 2014), vascular (van Meeteren et al., 2006) and neural development (Fotopoulou et al., 2010), and in tumor growth, metastasis (Leblanc and Peyruchaud, 2015) and chemoresistance (Brindley et al., 2013).

Consequently, ATX is a potential therapeutic target in various diseases, including cancer, as the ATX-LPA signaling axis plays a role in various tumor types (Houben and Moolenaar, 2011; Liu et al., 2009). Noteworthy, the ENPP2 gene itself, is amplified in tumors of the breast (8.2%), the ovary (6.9%), the eye (6.3%) and the liver (4.6%) (Fig. 1) (“COSMIC,” 2016). In addition, genetic silencing of ATX and LPA receptors expression in mouse models reveals the importance of ATX-LPA axis in cancer development (Liu et al., 2009). Being an extracellular enzyme, ATX represents an attractive drug target and there is potential for designing novel small-molecule inhibitors targeting this enzyme. Moreover, pharmacologic inhibition of ATX is well tolerated, at least in adult mice (Katsifa et al., 2015).

To date, efforts to target ATX have disclosed small-molecule inhibitors (reviewed in ref. Castagna et al., 2016), as well as an aptamer (Kato et al., 2016). The field is still relatively young, as so far only one ATX inhibitor, GLPG1690 (Fig. 2), has been reported to be in clinical trials (“Galapagos NV,” 2000) and is currently on phase II for patients with idiopathic pulmonary fibrosis. In general, most of the reported ATX inhibitors display similar chemotype, consisting of three elements: an acidic moiety, a spacer core and a lipophilic tail (Castagna et al., 2016). The acidic headgroup binds to  $Zn^{2+}$ -ions in the active site and the core spacer guides the hydrophobic tail to the lipophilic pocket. However, a few inhibitors have been discovered which do not follow this typical pattern. These inhibitors were identified to target only the lipophilic pocket or the tunnel, excluding the active site (Fells et al., 2013; Stein et al., 2015). With this type of inhibitors, Stein et al. demonstrated inhibitory action only towards ATX lysoPLD activity; moreover, Fells et al. demonstrated that their inhibitors reduced invasion and metastasis *in vitro*, truly disclosing the potential for inhibitors blocking only the pocket site. Moreover, Shah et al. published imidazo[4,5-*c*]pyridines series which bind to this site as well (Shah et al., 2016). Most recently, a SAR study identified an inhibitor which binds to the tunnel site (Miller et al., 2017), and benzene-sulfonamide derivatives were reported to reduce melanoma metastasis *in vivo* (Banerjee et al., 2017). Overall, this type of ATX inhibition, excluding the active-site binding which contains two  $Zn^{2+}$ -ions, will lower the potential risk in

off-target metalloprotein binding; for instance, similar tactics has been utilized in selective matrix-metalloproteinase inhibitor design (Jacobsen et al., 2010).

Herein, we disclose novel 2,4- dihydropyrano[2,3-*c*]pyrazoles that inhibit human ATX (hATX). Our results demonstrate and further support previous findings showing that a desired biological action can be achieved without targeting the catalytic site of the enzyme. Moreover, this study validated hen egg white ATX (ewATX) activity assay as a convenient and truly affordable method for initial discovery of ATX inhibitors. Noteworthy, molecular modeling was able to correctly predict the biologically active enantiomer of the 2,4- dihydropyrano[2,3-*c*]pyrazoles, as verified by compound crystallization and biological testing.

## 2. Material and Methods

### 2.1. Molecular modelling

#### 2.1.1. Virtual screening

We utilized following libraries in the virtual screening: ChemBridge, druglike and leadlike screening compounds (“ChemBridge Corporation,” 2014); Enamine, low molecular weight organic compounds - diverse drug like compounds (“Enamine Ltd,” 2014); Institute for Molecular Medicine Finland (FIMM), chemical collection of drugs and drug-like compounds ready to use for screening (“FIMM,” 2007); Maybridge, a highly diverse set of hit-like and lead-like molecules (“Maybridge,” 2014). The compounds were prepared with LigPrep 3.1 (“LigPrep,” 2014) using OPLS-2005 force field (Banks et al., 2005). All possible ionization states were generated at pH range 5.0-9.0 using Epik (“Epik,” 2014; Greenwood et al., 2010; Shelley et al., 2007), with metal binding states, including original state, and tautomers. Generation of stereoisomers were limited up to 10 and low energy ring conformation to one per ligand. For virtual screening a *Mus musculus* crystal structure (PDB ID: 3WAX) with 1.9 Å resolution was downloaded from Protein Data Bank. The structure was prepared using Protein Preparation Wizard (Sastry et al., 2013; “Schrödinger Suite 2014-3 Protein Preparation Wizard,” 2014) using default settings. Missing hydrogens and sidechains were added, hydrogen bond network was optimized and the structure was minimized with OPLS-2005 force field (Banks et al., 2005). Crystal waters No. 1245 and No. 1327 were preserved. Glide (Friesner et al., 2006, 2004; “Glide,” 2014; Halgren et al., 2004) module of Schrödinger Maestro software package (“Maestro,” 2015, “Maestro,” 2014) was used for docking. The Glide-grid was generated using default settings, allowing hydroxyl groups of S169 and Y306 to rotate. The grid-box was defined by a ligand from a docking pose of one of docked Ono Pharmaceuticals’ compound (Ohata et al., 2012). The docking model was validated using the co-crystallized ligand and the known inhibitors HA155 (Albers et al., 2010), PF8380 (Gierse et al., 2010), and compounds by Ono Pharmaceutical Co. Ltd. (Ohata et al., 2012). Physicochemical descriptors for the XP results were calculated by Canvas 2.1 (“Canvas,” 2014) and the results were filtered by AlogP <7, >0; hydrogen bond acceptors <7 and hydrogen bond donors <5. Clustering of the ligands was conducted with Pose Explorer script of Maestro (“Maestro,” 2014), using 2D Fingerprints. The IFD (Farid et al., 2006; “Induced Fit Docking,” 2015; Sherman et al., 2006a, 2006b) was conducted with XP precision using default 5 Å radius of Prime refinement for the residues. QM-polarized ligand docking (Cho et al., 2005;

“QM-Polarized Ligand Docking protocol,” 2015) was conducted with XP precision in initial docking, the QM charges were calculated with Jaguar (Bochevarov et al., 2013) fast, and XP precision was used in the redocking.

### 2.1.2. Hydration site analysis

Analysis was conducted with WaterMap (Abel et al., 2008; “WaterMap,” 2015; Young et al., 2007). The 3WAX structure (Kawaguchi et al., 2013), was prepared with Protein Preparation Wizard (“Protein Preparation Wizard,” 2015) (as above), except minimization was conducted with OPLS3 force field (Harder et al., 2016). Waters were analyzed within 8 Å of the co-crystallized ligand, and the 2 ns simulation was conducted with OPLS3 force field.

### 2.1.3. Interaction analysis

The interactions of published ATX crystal structures in complex with inhibitors were analyzed after default protein preparation with PrepWiz with OPLS3 force field. The graphical illustrations were created with Maestro (“Maestro,” 2016) (Fig. 6) and PyMOL (“PyMOL,” 2016) (Fig. 7).

## 2.2. X-ray Structure Determination of Compounds (S)-**18**, (R)-**19**, (S)-**23** and (S)-**25**

Enantiomerically pure compounds **18**, **19**, **23** and **25** were crystallized at 298 K by slow evaporation of their acetonitrile/water, ethanol/heptane, ethanol/water and methanol/dibutyl ether solutions, respectively. Suitable crystals were immersed in cryo-oil, mounted in a Nylon loop, and measured at a temperature of 150 K. The X-ray diffraction data was collected on a Bruker Kappa Apex II Duo diffractometer using CuK $\alpha$  radiation ( $\lambda = 1.54178$  Å). The APEX2 program (“APEX2,” 2010) package was used for cell refinements and data reductions. The structures were solved by direct methods using the SHELXS-2014 programs (Sheldrick, 2015) with the WinGX graphical user interface (Farrugia, 2012). A semi-empirical absorption correction (SADABS) (Sheldrick, 2008) was applied to all data. Structural refinements were carried out using SHELXL-2014 (Sheldrick, 2015).

Some dichlorophenyl groups in **19** and **23** were disordered between two positions and were refined with occupancies of 0.65/0.35 and 0.58/0.42, respectively. A series of geometry and displacement constraints and restraints were applied to these moieties.

The crystallization solvent molecules were partially lost from the crystals of **18** (acetonitrile) and **25** (dibutyl ether) and therefore were refined with 0.5 occupancy. In addition, crystallization solvent in **19** and **23** could not be resolved unambiguously and its contribution to the calculated structure factors was taken into account by using a *SQUEEZE* routine of *PLATON* (Spek, 2013). The missing solvent was not taken into account in the unit cell content.

The NH and NH<sub>2</sub> hydrogen atoms were located from the difference Fourier map but constrained to ride on their parent atoms, with  $U_{\text{iso}} = 1.2\text{--}1.5 U_{\text{eq}}$  (parent atom). All hydrogen atoms were positioned geometrically and constrained to ride on their parent atoms, with C-H = 0.95–1.00 Å, and  $U_{\text{iso}} = 1.2\text{--}1.5 U_{\text{eq}}$  (parent atom).

Analysis of the absolute configurations of **18**, **19**, **23** and **25** using likelihood methods (Hoofst et al., 2008) was performed using *PLATON* (Spek, 2013). The absolute structure parameter  $\gamma$  was calculated to yield 0.009(6) for **18**, 0.036(4) for **19**, 0.060(11) for **23**, 0.005(8) for **25**, indicating that the absolute structures (**18**, *S*; **19**, *R*; **23**, *S*; **25**, *S*) very likely have been determined correctly. The Flack  $x$  parameter was refined to give the values of 0.03(2) for **18**, 0.01(1) for **19**, 0.01(3) for **23**, 0.010(7) for **25**, that also corresponds to a correct absolute structure determination. The crystallographic details are summarized in Suppl. Table S3.

### 2.3. Biological assays

#### 2.3.1. Chemicals and Reagents

All chemicals used in the biological assays were of highest available purity. LPC (L- $\alpha$ -lysophosphatidylcholine from egg yolk; Sigma-Aldrich, Cat# 62962, lotBCBD9043V, MW 299.26 g/mol, Purity  $\geq 99.0\%$ ) was dissolved in methanol (JT Baker #8402) as a stock solution of 167 mM LPC. Horseradish peroxidase (HRP; Sigma-Aldrich, Cat# P8125, lot#108K7351V, 5000U) was dissolved in Millipore water (high quality water, HQW) to make 250 U/ml HRP stock. Choline Oxidase (CO; Sigma-Aldrich, Cat# C5896, MW. ~95 kDa) derived from *Alcaligenes* sp. was purchased as lyophilized powder, dissolved in HWQ as 65 U/ml stock and aliquoted for storage at -80 °C. A 10 mM Amplex Red (Sigma-Aldrich, Cat# 90101-5MG-F lot#BCBK4832V, Purity  $\geq 98.0\%$ ) solution was prepared in DMSO and aliquoted for storage at -80 °C. The artificial ATX substrate pNP-TMP (thymidine 5'-monophosphate *p*-nitrophenyl ester sodium salt, Sigma-Aldrich, cat T4510, MW 465.28 g/mol, Purity  $\geq 98\%$ )

(HPLC)) was dissolved in HQW as 100 mM stock solution and aliquoted for storage at -80 °C. The reference inhibitors HA155 (B-[4-[[4-[(Z)-[3-[(4-fluorophenyl)methyl]-2,4-dioxo-5-thiazolidinylidene]methyl]phenoxy]methyl]phenyl]boronic acid), Sigma-Aldrich, Cat# SML0914, MW. 463.29, Purity  $\geq$ 98% (HPLC)), PF8380 (4-[3-(2,3-dihydro-2-oxo-6-benzoxazolyl)-3-oxopropyl]-1-piperazinecarboxylic acid (3,5-dichlorophenyl)methyl ester, Sigma-Aldrich, Cat# SML0715, Lot# 103M4746V, MW. 478.33, Purity  $\geq$ 98% (HPLC)), and S32826 (P-[[4-[(1-oxotetradecyl)amino]phenyl]methyl]-phosphonic acid, Cayman, Cat#13664, MW 397.5, Purity  $\geq$ 98%) were purchased as dry powder and 10 mM stock solutions were prepared in DMSO and aliquoted for storage at -80 °C. We have tested total of 85 compounds in the entire screening assays, collected from different sources as dry matter and dissolved in DMSO as 10 mM stock solutions and aliquoted for storage at -80 °C. From the inhibitors, compounds **3-17** were purchased from different commercial providers: compounds **3-5** and **7-17** from Vitas-M Laboratory, Champaign, IL 61820, USA, compound **6** from Specs, Zoetermeer, The Netherlands. Compounds **1-2** were obtained from Institute for Molecular Medicine Finland (FIMM), Helsinki, Finland. A total of 11 compounds (compounds **18-28**) were synthesized locally at the School of Pharmacy, Faculty of Health Sciences, University of Eastern Finland (see Chemistry).

Recombinant Human ENPP-2/ATX was purchased from R&D Systems (Acc#Q13822, Lot RPZ101511A, total amount 500  $\mu$ g; purity  $>$ 95%; specific activity  $>$  8000 pmoles/min/ $\mu$ g). The enzyme was supplied as 299  $\mu$ l of a 0.2 mm filtered solution in 25 mM Tris and 150 mM NaCl, pH 7.5 at a concentration of 1.690 mg/ml. Upon arrival, the enzyme preparation was thawed and a 60  $\mu$ l-aliquot was diluted by adding 256  $\mu$ l of 5% (w/v) BSA plus 384  $\mu$ l of HQW to give total volume of 700  $\mu$ l. This was mixed, spun briefly to force all liquid to the bottom, and divided in 20 x 35.0  $\mu$ l aliquots for storage at -80 °C. We used one aliquot (35  $\mu$ l) per experiment with 48 wells (half of a 96-well plate).

### 2.3.2. Cell Culture

Human melanoma cell line A2058 (American Type Culture Collection, ATCC) was grown in complete DMEM medium (Gibco, high glucose) supplemented with 10% (v/v) fetal bovine serum (FBS; EuroClone) and 2 mM L-glutamine. Cells were grown in 5% CO<sub>2</sub> containing humidified incubator at 37 °C. For migration, sub-confluent A2058 cells were washed with 1xPBS and treated with 0.05% trypsin/0,02% EDTA in phosphate-buffer saline (PBS; EuroClone) followed by suspending into serum-free DMEM media having 0.5x10<sup>5</sup> cells/ml. Exactly 500



$\mu$ l of cell suspension was added in each migration chamber to give 25,000 cells per insert per sample. No antibiotics were used during the cell culture period.

### 2.3.3. Hen Egg White ATX Preparation

The hen egg white was separated from an unfertilized egg, purchased from local grocery store, into a 50 ml conical tube (original volume 45 ml) and stored overnight at  $-20^{\circ}\text{C}$ . Later it was thawed, vortexed gently, and stored in aliquots for future use at  $-20^{\circ}\text{C}$ . The egg white was diluted 1:5 with saline. For assay blank, heat-inactivated EW 1:5 (HI-EW 1:5) was prepared as 1:5 dilution of original EW. A magnetic stirrer was used to mix EW with saline while heating at  $56^{\circ}\text{C}$  for 10 minutes. The preparation was then cooled down, aliquoted, and stored at  $-20^{\circ}\text{C}$ .

### 2.3.4. Choline Release Assay

The methodology was adapted from a previous publication by Ferry et al., 2008[53]. Briefly, we have used black 96-well-plates suitable for fluorescence measurements. The final reaction volume was 200  $\mu$ l/well. The basic principle of this assay is that ATX catalyzes the hydrolysis of lysophosphatidylcholine (LPC) to generate LPA and choline. Choline oxidase-catalyzed oxidation of choline generates  $\text{H}_2\text{O}_2$  which in the presence of peroxidase converts Amplex Red into the fluorescent product Resorufin. Resorufin fluorescence was kinetically monitored at 30 min intervals for 90 min ( $\lambda_{\text{ex}}$  530;  $\lambda_{\text{em}}$  590 nm). For inhibitor screening, 1  $\mu$ l of DMSO/inhibitors with 100-fold desired final concentration was added first into the bottom of the appropriate well, followed by 99  $\mu$ l of enzyme, blank (HI-EW) or choline quality control (CQC)  $\pm$  inhibitor preparation in Co-CAB buffer. The Co-CAB buffer contained 50 mM Tris-HCl, pH 7.4, 5 mM  $\text{CaCl}_2$ , 1 mM  $\text{CoCl}_2$  and 0.1% (w/v) BSA as the final concentration per reaction. Following 30 min pre-incubation of the enzyme with inhibitors, 100  $\mu$ l of choline assay mix (CAM; containing 50 mM Tris-HCl pH 7.4, 5 mM  $\text{CaCl}_2$ , 1.0 mM  $\text{CoCl}_2$ , 0.1% (w/v) BSA, 200  $\mu$ M LPC, 1.0 U/ml horseradish peroxidase,  $\sim$ 0.52 U/ml choline oxidase, and 40  $\mu$ M Amplex Red as the final concentration per reaction) was added using a multichannel pipette; the plate was vortexed and the fluorescence was kinetically monitored at 30 min intervals for 90 min at  $37^{\circ}\text{C}$ . Extensive validation of the ewATX preparation was performed and the results of the validation studies are presented in S8-S12 in Suppl. Information.

### 2.3.5. *pNP-TMP Hydrolysis assay*

This assay was adapted and modified from previously published protocols (Kakugawa et al., 2015; Muccioli et al., 2008) and is based on the following principle: ATX-dependent hydrolysis of the chromogenic substrate pNP-TMP liberates pNP whose absorbance was colorimetrically monitored at 405 nm. In brief, the enzymatic hydrolysis was performed in a 96-well clear microplate (Greiner bio-one) where 1  $\mu$ l of DMSO/inhibitor (100-fold desired final concentration) was incubated at room temperature for 30 min with 99  $\mu$ l of enzyme or blank or pNP standard (49.5 nmol/well) prepared in Co-CAB buffer (50 mM Tris-HCl- pH 7.4, 5 mM CaCl<sub>2</sub>, 1 mM CoCl<sub>2</sub> and 0.1% (w/v) BSA). The 100  $\mu$ l of substrate mixture (500  $\mu$ M final concentration) was added per well, then the pNP absorbance ( $\lambda$  405 nm) was kinetically measured at 30 min intervals for 90 min at 37 °C using Tecan plate reader. The amount of pNP release per reaction was calculated based on the pNP standard.

### 2.3.6. *Cell Migration Assays*

Migration assay was carried out by using 8- $\mu$ m pore size polyethylene terephthalate (PET) membranes (Corning BioCoat Control Inserts for 24-well plates, Cat#354578) on human melanoma cell line (A2058), as it shows LPA dependent cell migration (Nam et al., 2000). The inserts were washed and filled with 500  $\mu$ l of cell suspension (total 25,000 cells per inserts) in serum free medium. The inserts with cells were placed into the 24-well plate containing 750  $\mu$ l of DMEM with 10% FBS as chemo-attractant along with ATX  $\pm$  inhibitors, and/or controls. The inserts were then incubated for 4 h at 37 °C in a humidified incubator containing 5% CO<sub>2</sub>, after which non-migrating cells were removed from the apical side of the membrane by swabbing/scraping with cotton swabs. Thereafter the membrane inserts with migrated cells were fixed in 100% methanol for 3 min, stained with Diff-Quick staining kit (Medion Diagnostics AG, Switzerland) according to manufacturer's instructions, and mounted onto glass slides for quantitative analysis (counting) by microscope. The cells were counted and averaged of eight different 10x magnified fields per samples. The experiments were repeated three times and data were analyzed statistically by using 1-way-ANOVA followed by Tukeys multiple comparisons with Graphpad Prism-5.

### 2.4. *Chemistry*

Reagents and solvents were purchased from commercial suppliers and were used without further purification. Most of the reactions were monitored by thin-layer chromatography (TLC) with suitable UV visualization. Purification was carried out by flash chromatography (FC) or by CombiFlash Companion (Teledyne Isco, USA).  $^1\text{H}$  NMR and  $^{13}\text{C}$  NMR were recorded on a Bruker Avance AV 500 (Bruker Biospin, Switzerland) spectrometer and processed from the recorded FID files with TOPSPIN 2.1 software or ACD/NMR Processor Academic Edition. The  $^1\text{H}$  NMR spectra were referenced to the residual proton impurities at  $\delta\text{H}$  2.50 ppm and 7.26 ppm in  $\text{DMSO-d}_6$  and  $\text{CDCl}_3$ , respectively. The  $^{13}\text{C}$  NMR spectra were referenced at  $\delta\text{C}$  39.52 and 77.00 ppm to  $\text{DMSO-d}_6$  and  $\text{CDCl}_3$ , respectively. ESI-MS spectra were acquired using an LCQ quadrupole ion trap mass spectrometer equipped with an electrospray ionization source (Thermo LTQ, San Jose, CA, USA). Elemental analyses were performed on a Thermo Quest CE Instruments EA1110- CHNS-O elemental analyzer or on a Perkin-Elmer PE 2400 Series II CHNS-O Analyzer. The purity of the compounds was determined either by elemental analysis or by HPLC and all compounds exhibited  $\geq 95\%$  purity, except for compound **28** which purity was 90% determined by qNMR analysis. The enantiomers of racemic compounds were separated by preparative HPLC (see Suppl. Information S24).

#### 2.4.1. General procedure for preparation of 6-amino-3-phenyl-4-(3,4-dichlorophenyl)-2,4-dihydropyrano[2,3-c]pyrazole-5-carbonitriles

A mixture of the 3,4-dichlorobenzaldehyde (1.0 equ.), malononitrile (1.0 equ.) and *N*-methylmorpholine (1.0 equ.) in ethanol is stirred for 1 min, followed by the addition of the appropriate 1*H*-pyrazol-5(4*H*)-one (see Suppl. Information). The precipitate formed was filtered out and washed with ethanol and *n*-hexane, and recrystallized from ethanol or purified by column chromatography.

#### 2.4.2. ( $\pm$ )-6-Amino-3-[3-(benzyloxy)phenyl]-4-(3,4-dichlorophenyl)-2,4-dihydropyrano[2,3-c]pyrazole-5-carbonitrile (**18**)

Prepared according to general procedure. The precipitate formed was filtered out, washed *n*-hexane, and dried in vacuum. The racemic compound **18** was obtained as a white solid (149 mg, 60%).  $^1\text{H}$  NMR (500 MHz,  $\text{DMSO-d}_6$ ):  $\delta$  12.94 (s, 1H), 7.46 (d,  $J = 8.4$  Hz, 1H), 7.36 - 7.45 (m, 4H), 7.33 (m, 1H), 7.25 (t,  $J = 8.3$  Hz, 1H), 7.00 - 7.09 (m, 5H), 6.93 (dd,  $J = 2.4, 8.6$  Hz, 2H), 5.12 (s, 1H), 5.08 (d,  $J = 11.9$  Hz, 1H), 4.96 (d,  $J = 11.9$  Hz, 1H).  $^{13}\text{C}$  NMR (125 MHz,  $\text{DMSO-d}_6$ )  $\delta$ : 160.2, 158.4, 155.8, 145.6, 138.0, 136.8, 130.71, 130.72, 129.8, 129.6, 129.3,

129.2, 128.4 (2C), 127.9, 127.6 (2C), 120.2 (CN), 118.9, 115.3, 112.4, 96.4, 69.3, 57.1, 35.6; ESI-MS 489.20 [M+H]<sup>+</sup>; Anal. Calcd for C<sub>26</sub>H<sub>18</sub>Cl<sub>2</sub>N<sub>4</sub>O<sub>2</sub>: C 63.82, H 3.71, N 11.45; found: C 63.41, H 3.68, N 11.34.

2.4.3.(-)-(R)-6-Amino-3-[3-(benzyloxy)phenyl]-4-(3,4-dichlorophenyl)-2,4-dihydropyrano[2,3-c]pyrazole-5-carbonitrile [(R)-**18**]: and (+)-(S)-6-Amino-3-[3-(benzyloxy)phenyl]-4-(3,4-dichlorophenyl)-2,4-dihydropyrano[2,3-c]pyrazole-5-carbonitrile [(S)-**18**]

The racemic compound **18** was separated using a chiral chromatography (Phenomenex column, acetonitrile/isopropyl alcohol (9:1) as the eluent). The retention time for enantiomer A was 10 min assigned as (-)-enantiomer with  $[\alpha]^{23}_D$  (c 0.7 MeCN) = -214. The retention time for enantiomer B was 13 min assigned as (+)-enantiomer with  $[\alpha]^{23}_D$  (c 0.04 MeCN) = +260. The absolute configuration of the second-eluted (+)-enantiomer **18** was to be *S* determined by X-ray crystallography.

2.4.4.(±)-6-Amino-3-[4-(benzyloxy)phenyl]-4-(3,4-dichlorophenyl)-2,4-dihydropyrano[2,3-c]pyrazole-5-carbonitrile (**19**)

Prepared according to general procedure. The precipitate formed was filtered out, washed *n*-hexane, and dried in vacuum. The racemic compound **19** was obtained as a white solid (230 mg, 88%). <sup>1</sup>H NMR (500 MHz, DMSO-d<sub>6</sub>): δ 12.78 (s, 1H), 7.45 (d, *J* = 8.5 Hz, 2H), 7.30 - 7.44 (m, 7H), 7.07 (dd, *J* = 2.0, 8.4 Hz, 1H), 7.01 (s, 2H), 6.96 (d, *J* = 8.5 Hz, 2H), 5.09 (s, 2H), 5.08 (s, 1H). <sup>13</sup>C NMR (125 MHz, DMSO-d<sub>6</sub>) δ: 160.3, 158.4, 155.6, 145.6, 138.1, 136.7, 130.7, 130.6, 129.3, 129.1, 128.4 (2C), 127.83, 127.80 (2C), 127.6 (2C), 121.0, 120.3 (CN), 114.9 (2C), 95.5, 69.2, 57.1, 35.6; ESI-MS 489.20 [M+H]<sup>+</sup>; Anal. Calcd for C<sub>26</sub>H<sub>18</sub>Cl<sub>2</sub>N<sub>4</sub>O×0.6 H<sub>2</sub>O: C 62.44, H 3.87, N 11.20; found: C 62.68, H 4.06, N 10.74.

2.4.5.(-)-(S)-6-Amino-3-[4-(benzyloxy)phenyl]-4-(3,4-dichlorophenyl)-2,4-dihydropyrano[2,3-c]pyrazole-5-carbonitrile [(S)-**19**]: and (+)-(R)-6-Amino-3-[4-(benzyloxy)phenyl]-4-(3,4-dichlorophenyl)-2,4-dihydropyrano[2,3-c]pyrazole-5-carbonitrile [(R)-**19**]

The racemic compound **19** was separated using a chiral chromatography (Phenomenex column, acetonitrile/isopropyl alcohol (9:1) as the eluent). The retention time for enantiomer A (compound (R)-**19** on Table 3) was 10 min assigned as (-)-enantiomer with  $[\alpha]^{23}_D$  (c 0.3 MeCN) = -280. The retention time for enantiomer B (compound (S)-**19** on Table 3) was 16 min assigned as (+)-enantiomer with  $[\alpha]^{23}_D$  (c 0.3 MeCN) =

+304. The absolute configuration of the first-eluted (-)-enantiomer **19** was found to be *R* assigned on the basis of an X-ray crystallographic analysis.

2.4.6.(±)-6-Amino-3-[2-(benzyloxy)phenyl]-4-(3,4-dichlorophenyl)-2,4-dihydropyrano[2,3-*c*]pyrazole-5-carbonitrile (**20**)

Prepared according to general procedure and purified by flash column chromatography (SiO<sub>2</sub>, gradient elution with 10 - 50% ethyl acetate in petroleum ether). The racemic compound **20** was obtained as a white solid (205 mg, 50%). <sup>1</sup>H NMR (500 MHz, DMSO-*d*<sub>6</sub>): δ 12.59 (s, 1H), 7.27 – 7.40 (m, 7H), 7.15 (dd, *J* = 1.7, 7.6 Hz, 1H), 7.08 (dd, *J* = 0.7, 8.3 Hz, 1H), 7.02 (d, *J* = 2.1 Hz, 1H), 6.99 (s, 2H), 6.86 – 6.92 (m, 2H), 5.19 (d, *J* = 12.2 Hz, 1H), 5.03 (d, *J* = 12.2 Hz, 1H), 4.77 (s, 1H). <sup>13</sup>C NMR (125 MHz, DMSO-*d*<sub>6</sub>) δ: 160.8, 155.3, 154.6, 145.3, 136.6, 136.1, 130.51, 130.47, 130.24, 130.15, 129.0, 128.8, 128.4 (2C), 127.9, 127.44, 127.35 (2C), 120.5, 120.2 (CN), 117.9, 112.8, 98.1, 69.6, 56.2, 36.1; ESI-MS 489.20 [M+H]<sup>+</sup>; Anal. Calcd for C<sub>26</sub>H<sub>18</sub>Cl<sub>2</sub>N<sub>4</sub>O × 0.5 H<sub>2</sub>O: C 62.66, H 3.84, N 11.24; found: C 62.97, H 4.28, N 11.69.

2.4.7.(-)-(*R*)-6-Amino-3-[2-(benzyloxy)phenyl]-4-(3,4-dichlorophenyl)-2,4-dihydropyrano[2,3-*c*]pyrazole-5-carbonitrile [(*R*)-**20**]: and (+)-(*S*)-6-Amino-3-[2-(benzyloxy)phenyl]-4-(3,4-dichlorophenyl)-2,4-dihydropyrano[2,3-*c*]pyrazole-5-carbonitrile [(*S*)-**20**]

The racemic compound **20** was separated using a chiral chromatography (Phenomenex column, acetonitrile/isopropyl alcohol (9:1) as the eluent). The retention time for enantiomer A was 8 min assigned as (-)-enantiomer with [α]<sup>23</sup>D (c 0.4 MeCN) = -254. The retention time for enantiomer B was 18 min assigned as (+)-enantiomer with [α]<sup>23</sup>D (c 0.5 MeCN) = +259.

2.4.8.(±)-6-Amino-4-(3,4-dichlorophenyl)-3-[4-(phenoxy)phenyl]-2,4-dihydropyrano[2,3-*c*]pyrazole-5-carbonitrile (**21**)

Prepared according to general procedure. The precipitate formed was filtered out, washed *n*-hexane, and dried in vacuum. The racemic compound **21** was obtained as a white solid (520 mg, 87%). <sup>1</sup>H NMR (500 MHz, DMSO-*d*<sub>6</sub>): δ 12.88 (s, 1H), 7.46 (d, *J* = 8.9 Hz, 2H), 7.46 (d, *J* = 8.3 Hz, 1H), 7.40 (dd, *J* = 7.4, 8.7 Hz, 2H), 7.35 (d, *J* = 2.1 Hz), 7.17 (tt, *J* = 1.1, 7.4 Hz, 1H), 7.06 (dd, *J* = 2.1, 8.4 Hz, 1H), 7.04 (s, 2H), 6.97 (dd, *J* = 1.1, 8.7 Hz, 2H), 6.93 (d, *J* = 8.9 Hz), 5.09 (s, 1H). <sup>13</sup>C NMR (125 MHz, DMSO-*d*<sub>6</sub>) δ: 160.4, 156.9, 156.0, 155.6, 145.4, 137.9, 130.6, 130.5, 130.1 (2C), 129.4, 129.1, 128.1 (2C), 127.8, 123.9, 123.5, 120.3 (CN), 118.9 (2C), 118.3 (2C),

96.3, 56.9, 35.6; ESI-MS 473.24 [M-H]<sup>-</sup>; Anal. Calcd for C<sub>25</sub>H<sub>16</sub>Cl<sub>2</sub>N<sub>4</sub>O<sub>2</sub>×0.67 H<sub>2</sub>O: C 61.61, H 3.59, N 11.46; found: C 62.00, H 3.96, N 11.05.

2.4.9.(-)-(R)-6-Amino-4-(3,4-dichlorophenyl)-3-[4-(phenoxy)phenyl]-2,4-dihydropyrano[2,3-c]pyrazole-5-carbonitrile [(R)-**21**]: and (+)-(S)-6-Amino-4-(3,4-dichlorophenyl)-3-[4-(phenoxy)phenyl]-2,4-dihydropyrano[2,3-c]pyrazole-5-carbonitrile [(S)-**21**]

The racemic compound **21** was separated using a chiral chromatography (Phenomenex column, acetonitrile/isopropyl alcohol (9:1) as the eluent). The retention time for enantiomer A was 10 min assigned as (-)-enantiomer with  $[\alpha]^{23}_D$  (c 0.1 MeCN) = -252. The retention time for enantiomer B was 15 min assigned as (+)-enantiomer with  $[\alpha]^{23}_D$  (c 0.1 MeCN) = +275.

2.4.10.(±)-6-Amino-4-(3,4-dichlorophenyl)-3-(3-phenoxyphenyl)-2,4-dihydropyrano[2,3-c]pyrazole-5-carbonitrile (**22**)

Prepared according to general procedure. The precipitate formed was filtered out, washed *n*-hexane, and dried in vacuum. The racemic compound **22** was obtained as a white solid (340 mg, 61%). <sup>1</sup>H NMR (500 MHz, DMSO-d<sub>6</sub>): δ 12.99 (s, 1H), 7.42 (d, *J* = 8.3 Hz, 1H), 7.39 (dd, *J* = 7.4, 8.7 Hz, 2H), 7.34 (t, *J* = 7.4 Hz, 1H), 7.26 (d, *J* = 2.1 Hz, 1H), 7.25 (m, 1H), 7.16 (tt, *J* = 1.1, 7.4 Hz, 1H), 7.07 (t, *J* = 2.1 Hz, 1H), 7.03 (s, 2H), 6.97 (dd, *J* = 2.1, 8.4 Hz, 1H), 6.89 – 6.92 (m, 3H), 5.02 (s, 1H). <sup>13</sup>C NMR (125 MHz, DMSO-d<sub>6</sub>): δ: 160.3, 156.7, 156.3, 155.7, 145.3, 137.5, 130.8, 130.6, 130.4, 130.1, 130.0 (2C), 129.21, 129.19, 127.6, 123.6, 121.7, 120.2 (CN), 118.7 (2C), 118.5, 116.7, 96.7, 57.0, 35.6; ESI-MS 473.25 [M-H]<sup>-</sup>; Anal. Calcd for C<sub>25</sub>H<sub>16</sub>Cl<sub>2</sub>N<sub>4</sub>O<sub>2</sub>: C 63.17, H 3.39, N 11.79; found: C 63.15, H 3.29, N 11.72.

2.4.11.(-)-(R)-6-Amino-4-(3,4-dichlorophenyl)-3-(3-phenoxyphenyl)-2,4-dihydropyrano[2,3-c]pyrazole-5-carbonitrile [(R)-**22**]: and (+)-(S)-6-Amino-4-(3,4-dichlorophenyl)-3-(3-phenoxyphenyl)-2,4-dihydropyrano[2,3-c]pyrazole-5-carbonitrile [(S)-**22**]: (**22**)

The racemic compound **22** was separated using a chiral chromatography (Phenomenex column, acetonitrile/isopropyl alcohol (9:1) as the eluent). The retention time for enantiomer A was 9 min assigned as (-)-enantiomer with  $[\alpha]^{23}_D$  (c 0.9 MeCN) = -240. The retention time for enantiomer B was 13 min assigned as (+)-enantiomer with  $[\alpha]^{23}_D$  (c 0.7 MeCN) = +249.

2.4.12.(±)-6-Amino-4-(3,4-dichlorophenyl)-3-(2-phenoxyphenyl)-2,4-dihydropyrano[2,3-*c*]pyrazole-5-carbonitrile (**23**)

Prepared according to general procedure and purified by flash column chromatography (SiO<sub>2</sub>, gradient elution with 10 - 60% ethyl acetate in petroleum ether. The racemic compound **23** was obtained as a slightly yellow solid (152 mg, 24%). <sup>1</sup>H NMR (500 MHz, DMSO-d<sub>6</sub>): δ 12.73 (s, 1H), 7.39 (d, *J* = 8.2 Hz, 2H), 7.36 (ddd, *J* = 1.7, 7.5, 8.2 Hz, 1H), 7.27 (dd, *J* = 7.4, 8.6 Hz, 2H), 7.16 (td, *J* = 1.1, 7.5 Hz, 1H), 7.13 (d, *J* = 2.1 Hz, 1H), 7.06 (t, *J* = 6.9 Hz, 1H), 7.03 (s, 2H), 6.96 (dd, *J* = 8.4 Hz, 1H), 6.87 (dd, *J* = 1.0, 8.3 Hz, 1H), 6.62 (d, *J* = 7.6 Hz, 2H), 4.94 (s, 1H). <sup>13</sup>C NMR (125 MHz, DMSO-d<sub>6</sub>) δ: 160.8, 156.3, 154.5, 153.2, 145.2, 135.1, 131.0, 130.8, 130.6, 130.3, 129.8 (2C), 129.3, 129.0, 127.7, 123.8, 123.2, 120.8, 120.3 (CN), 119.3, 117.6 (2C), 98.3, 56.1, 35.9. ESI-MS 473.25 [M-H]<sup>-</sup>; Anal. Calcd for C<sub>25</sub>H<sub>16</sub>Cl<sub>2</sub>N<sub>4</sub>O<sub>2</sub>×0.1 H<sub>2</sub>O: C 62.93, H 3.42, N 11.73; found: C 62.74, H 3.56, N 11.49.

2.4.13.(-)-(R)-6-Amino-4-(3,4-dichlorophenyl)-3-(2-phenoxyphenyl)-2,4-dihydropyrano[2,3-*c*]pyrazole-5-carbonitrile [(R)-**23**]: and (+)-(S)-6-Amino-4-(3,4-dichlorophenyl)-3-(2-phenoxyphenyl)-2,4-dihydropyrano[2,3-*c*]pyrazole-5-carbonitrile [(S)-**23**]:

The racemic compound **23** was separated using a chiral chromatography (Phenomenex column, acetonitrile/isopropyl alcohol (9:1) as the eluent). The retention time for enantiomer A was 8 min assigned as (-)-enantiomer with [α]<sup>23</sup>D (c 0.7 MeCN) = -220. The retention time for enantiomer B was 12 min assigned as (+)-enantiomer with [α]<sup>23</sup>D (c 1.1 MeCN) = +208. The absolute configuration of the second-eluted (+)-enantiomer **23** was to be *S* determined by X-ray crystallography.

2.4.14.(±)-6-Amino-3-(4-[(4-chlorobenzyl)oxy]phenyl)-4-(3,4-dichlorophenyl)-2,4-dihydropyrano[2,3-*c*]pyrazole-5-carbonitrile (**24**)

Prepared according to general procedure and purified by flash column chromatography (SiO<sub>2</sub>, gradient elution with 50 - 100% ethyl acetate in petroleum ether. The racemic compound **24** was obtained as a Slightly yellow solid (148 mg, 35%). <sup>1</sup>H NMR (500 MHz, DMSO-d<sub>6</sub>): δ 12.79 (s, 1H), 7.73 - 7.46 (m, 4H), 7.40 (d, *J* = 8.8 Hz, 2H), 7.34 (d, *J* = 2.1 Hz, 1H), 7.06 (dd, *J* = 2.1, 8.9 Hz, 1H), 7.02 (s, 2H), 6.95 (d, *J* = 8.8 Hz, 2H), 5.09 (s, 2H), 5.09 (s, 1H). <sup>13</sup>C NMR (125 MHz, DMSO-d<sub>6</sub>) δ: 160.3, 158.2, 155.6, 145.6, 138.1, 135.8, 132.4, 130.7, 130.6, 129.5 (2C), 129.3, 129.1, 128.4 (2C), 127.8 (2C), 127.7, 120.2, 120.3 (CN), 114.9 (2C), 95.6, 68.3, 57.1,

35.6; ESI-MS 521.18 [M-H]<sup>+</sup>; Anal. Calcd for C<sub>26</sub>H<sub>17</sub>Cl<sub>3</sub>N<sub>4</sub>O<sub>2</sub> × 0.85 H<sub>2</sub>O: C 59.62, H 3.27, N, 10.70; found: C 58.25, H 3.44, N 10.90.

2.4.15.(-)-(R)-6-Amino-3-(4-[(4-chlorobenzyl)oxy]phenyl)-4-(3,4-dichlorophenyl)-2,4-dihydropyrano[2,3-c]pyrazole-5-carbonitrile [(R)-**24**]: and (+)-(S)-6-Amino-3-(4-[(4-chlorobenzyl)oxy]phenyl)-4-(3,4-dichlorophenyl)-2,4-dihydropyrano[2,3-c]pyrazole-5-carbonitrile [(S)-**24**]:

The racemic compound **24** was separated using a chiral chromatography (Phenomenex column, acetonitrile/isopropyl alcohol (9:1) as the eluent). The retention time for enantiomer A was 6 min assigned as (-)-enantiomer with [α]<sup>23</sup>D (c 0.7 MeCN) = -280. The retention time for enantiomer B was 10 min assigned as (+)-enantiomer with [α]<sup>23</sup>D (c 0.7 MeCN) = +287.

2.4.16.(±)-6-Amino-3-(4-[(4-fluorobenzyl)oxy]phenyl)-4-(3,4-dichlorophenyl)-2,4-dihydropyrano[2,3-c]pyrazole-5-carbonitrile (**25**)

Prepared according to general procedure. The precipitate formed was filtered out, washed *n*-hexane, and dried in vacuum. The racemic compound **25** was obtained as a white solid (54 mg, 43%). <sup>1</sup>H NMR (500 MHz, DMSO-d<sub>6</sub>): δ 12.79 (s, 1H), 7.47 (dd, *J* = 5.7, 8.9 Hz, 2H), 7.45 (d, *J* = 8.4 Hz, 1H), 7.40 (d, *J* = 8.9 Hz, 2H), 7.34 (d, *J* = 2.1 Hz, 1H), 7.21 (t, *J* = 8.9 Hz, 2H), 7.07 (dd, *J* = 2.1, 8.4 Hz, 1H), 7.02 (s, 2H), 6.95 (d, *J* = 8.9 Hz, 2H), 5.09 (s, 1H), 5.07 (s, 2H). <sup>13</sup>C NMR (125 MHz, DMSO-d<sub>6</sub>): δ: 161.8 (d, *J* = 244.0 Hz), 160.3, 158.3, 155.7, 145.6, 133.0 (d, *J* = 3.1 Hz), 130.7, 130.6, 130.0 (d, *J* = 8.0 Hz), 129.9, 129.3, 129.1, 127.8 (2C), 127.7, 120.1, 120.3 (CN), 115.0 (d, *J* = 21.4 Hz), 114.9 (2C), 95.5, 68.5, 57.1, 35.6; ESI-MS 505.21 [M-H]<sup>-</sup>; Anal. Calcd for C<sub>26</sub>H<sub>17</sub>Cl<sub>2</sub>FN<sub>4</sub>O<sub>2</sub> × 1.8 H<sub>2</sub>O: C 57.85, H 3.85, N 10.38; found: C 58.25, H 3.44, N 9.99.

2.4.17.(-)-(R)-6-Amino-3-(4-[(4-fluorobenzyl)oxy]phenyl)-4-(3,4-dichlorophenyl)-2,4-dihydropyrano[2,3-c]pyrazole-5-carbonitrile [(R)-**25**]: and (+)-(S)-6-Amino-3-(4-[(4-fluorobenzyl)oxy]phenyl)-4-(3,4-dichlorophenyl)-2,4-dihydropyrano[2,3-c]pyrazole-5-carbonitrile [(S)-**25**]

The racemic compound **25** was separated using a chiral chromatography (Phenomenex column, acetonitrile/isopropyl alcohol (9:1) as the eluent). The retention time for enantiomer A was 6 min assigned as (-)-enantiomer with [α]<sup>23</sup>D (c 0.4 MeCN) = -289. The retention time for enantiomer B was 9 min assigned as (+)-enantiomer with [α]<sup>23</sup>D (c 0.3 MeCN) = +309. The absolute configuration of the second-eluted (+)-enantiomer **25** was found to be *S* assigned on the basis of an X-ray crystallographic analysis.



2.4.18.(±)-6-Amino-4-(3,4-dichlorophenyl)-3-(4-[5-(4-fluorophenyl)-1H-pyrazol-1-yl]phenyl)-2,4-dihydropyrano[2,3-*c*]pyrazole-5-carbonitrile (**26**)

Prepared according to general procedure. The precipitate formed was filtered out, washed *n*-hexane, and dried in vacuum. White solid (160 mg, 48%). <sup>1</sup>H NMR (500 MHz, DMSO-*d*<sub>6</sub>): δ 13.00 (s, 1H), 7.76 (d, *J* = 1.8, 1H), 7.52 (d, *J* = 8.6 Hz, 2H), 7.44 (d, *J* = 8.3 Hz, 2H), 7.37 (d, *J* = 2.1 Hz, 1H), 7.14 – 7.23 (m, 6H), 7.06 (s, 2H), 7.06 (dd, *J* = 2.1, 8.6 Hz, 1H), 6.65 (d, *J* = 1.7, 1H), 5.15 (s, 1H). <sup>13</sup>C NMR (125 MHz, DMSO-*d*<sub>6</sub>) δ: 161.9 (d, *J* = 246.8 Hz), 160.2, 155.7, 145.3, 141.5, 140.5, 139.2, 137.3, 130.7 (d, *J* = 7.9 Hz, 2C), 130.6, 129.4, 129.1, 127.8, 127.3, 127.1 (2C), 126.41, 126.39, 124.9 (2C), 120.2 (CN), 115.6 (d, *J* = 21.9 Hz), 108.4, 96.8, 56.9, 35.5; ESI-MS 543.21 [M-H]<sup>+</sup>; Anal. Calcd for C<sub>28</sub>H<sub>17</sub>Cl<sub>2</sub>FN<sub>6</sub>O×0.3 H<sub>2</sub>O: C 61.89, H 3.15, N, 15.47; found: C 61.28, H 3.23, N 15.32.

2.4.19.(±)-6-Amino-4-(3,4-dichlorophenyl)-3-[4-(3-methyl-5-phenyl-1H-pyrazol-1-yl)phenyl]-2,4-dihydropyrano[2,3-*c*]pyrazole-5-carbonitrile (**27**)

Prepared according to general procedure. The precipitate formed was filtered out, washed *n*-hexane, and dried in vacuum. Slightly yellow solid (196 mg, 48%). <sup>1</sup>H NMR: (500 MHz, DMSO-*D*<sub>6</sub>) δ 12.97 (s, 1H), 7.48 (d, *J* = 8.6 Hz, 2H), 7.44 (d, *J* = 8.3 Hz, 1H), 7.33-7.37 (m, 2H), 7.31 (t, *J* = 7.4 Hz, 1H), 7.13 (m, 2H), 7.15 (d, *J* = 8.6 Hz, 2H), 7.05 (dd, *J* = 2.1, 8.1 Hz, 1H), 7.05 (s, 2H), 6.44 (s, 1H), 5.13 (s, 1H), 2.26 (s, 3H). <sup>13</sup>C NMR (125 MHz, DMSO-*d*<sub>6</sub>) δ: 160.2, 155.7, 148.9, 145.3, 143.1, 139.4, 137.4, 130.5, 130.1, 129.4, 129.1, 128.5, 128.2 (2C), 128.32, 128.28 (2C), 127.8 (2C), 126.9, 126.8, 124.6 (2C), 120.2 (CN), 108.3, 96.6, 57.0, 35.5, 13.3; ESI-MS 539.24 [M-H]<sup>+</sup>

2.4.20.Enantiomers A and B of 6-amino-4-(3,4-dichlorophenyl)-3-[4-(3-methyl-5-phenyl-1H-pyrazol-1-yl)phenyl]-2,4-dihydropyrano[2,3-*c*]pyrazole-5-carbonitrile (**27**)

The racemic compound **27** was separated using a chiral chromatography (Phenomenex column, acetonitrile/isopropyl alcohol (9:1) as the eluent). The retention time for enantiomer A was 8 min and the retention time for enantiomer B was 32 min. The specific rotations could not be determined due to low solubility.

2.4.21.(±)-6-Amino-3-(4-[4-(4-chlorophenyl)-1H-pyrazol-1-yl]phenyl)-4-(3,4-dichlorophenyl)-2,4-dihydropyrano[2,3-*c*]pyrazole-5-carbonitrile (**28**)

Prepared according to general procedure and purified by flash column chromatography (SiO<sub>2</sub>, gradient elution with 25 - 100% ethyl acetate in petroleum ether. Slightly yellow solid (24 mg, 13%). <sup>1</sup>H NMR (500 MHz, DMSO-d<sub>6</sub>): δ 13.02 (s, 1H), 9.09 (s, 1H), 8.26 (s, 1H), 7.85 (d, *J* = 8.7 Hz, 2H), 7.75 (d, *J* = 8.5 Hz, 2H), 7.64 (d, *J* = 8.7 Hz, 2H), 7.47 (d, *J* = 8.5 Hz, 2H), 7.47 (m, 1H), 7.41 (d, *J* = 2.0 Hz, 1H), 7.12 (dd, *J* = 1.9, 8.4 Hz, 1H), 7.07 (s, 2H), 5.21 (s, 1H); <sup>13</sup>C NMR (125 MHz, DMSO-d<sub>6</sub>): δ 160.3, 155.9, 145.6, 139.1, 139.1, 137.5, 131.1, 130.8, 130.8, 130.7, 129.4, 129.3, 128.9 (2C), 127.8, 127.6 (2C), 127.0 (2C), 126.2, 125.0, 123.3, 120.4 (CN), 118.0 (2C), 96.5, 57.1, 35.6 ; ESI-MS 557.22 [M-H] <sup>-</sup>; The purity of **28** as measured by qNMR was 90% (see Suppl. Information S23).

### 3. Results and Discussion

#### 3.1. *In silico* screening of novel ATX inhibitors

In order to identify novel ATX inhibitors, we conducted a virtual screening of 2.7 million compounds using Glide (Friesner et al., 2006, 2004; “Glide,” 2014; Halgren et al., 2004) of Schrödinger Maestro software package (“Maestro,” 2015, “Maestro,” 2014) (Fig. 3). As at the time no human ATX (hATX) structures were available, we used a reasonable quality *Mus musculus* crystal structure 3WAX (Kawaguchi et al., 2013) for virtual screening. The mouse Autotaxin (mATX) structure is highly similar with hATX with fully conserved amino acid composition in the substrate binding site (Suppl. Fig. S1-2). Utilizing the mATX structure, we generated and validated our docking model based on the co-crystallized ligand and the known inhibitors HA155 (Albers et al., 2010), PF8380 (Gierse et al., 2010) (Fig. 2), and patented compounds from Ono Pharmaceutical Co. Ltd. (Ohata et al., 2012). To construct a screening database, we prepared the ligands of four different libraries using LigPrep (“LigPrep,” 2014), to obtain all plausible tautomers, protomers and chiralities. Next, the prepared 11,817,620 structures were docked using high-throughput virtual screening (HTVS) precision of Glide. Furthermore, 2,095,000 molecules were docked using computationally more demanding standard precision (SP). Finally, the best 1,000 molecules from each of the four libraries were docked with extra precision (XP). These XP-results were filtered by Canvas (“Canvas,” 2014) in order to remove compounds with clearly non-drug-like properties (see Fig. 3). After filtering, the best 250 docking poses from each library were visually evaluated, and from these, 89 reasonable poses remained. Subsequently, the 89 compounds were clustered using 2D fingerprints, and 67 representative compounds were selected from the clusters. The 67 compounds were further docked by Induced Fit Docking (IFD) (Farid et al., 2006; “Induced Fit Docking,” 2015; Sherman et al., 2006a, 2006b), which treats the nearby residues within 5 Å of the binding ligand as flexible, using XP precision. Based on the IFD results, 26 compounds were selected to be tested for ATX inhibition in biological assays.

### 3.2. Hen egg-white ATX inhibition screening assay for the selected compounds

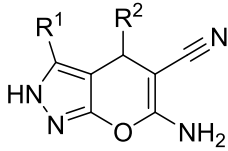
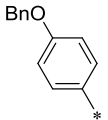
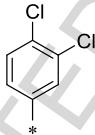
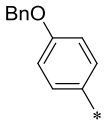
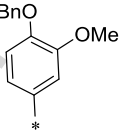
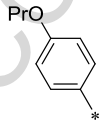
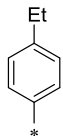
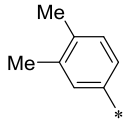
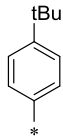
In 2001, Nakane et al. (Nakane et al., 2001) reported that hen egg white contains both LPC and an enzyme that catalyzes LPC hydrolysis to a corresponding polyunsaturated fatty acid-rich LPA. Later, the same group confirmed that ATX activity is responsible for LPA production in hen egg-white (Morishige et al., 2007). We were interested to broaden the utility of ewATX preparation and noticed that the amino acid sequences of human and hen ENPP2 display 83% identity, and from the pocket residues, only L260 is substituted with I260 in hen (Suppl. Fig. S3). Thus, the ewATX possesses a highly similar pocket with hATX and could therefore be utilized as an initial screening assay in the discovery of ATX inhibitor. We wished to further validate this preparation and by doing so established optimal conditions for ATX activity assays (detailed in Suppl. Information S8-S12). Briefly, optimal LPC hydrolytic activity was observed at 37 °C for 1:5 ewATX preparation diluted in saline, and in a buffer system consisting of 50 mM Tris-HCl, pH 7.4, 5 mM CaCl<sub>2</sub>, 1 mM CoCl<sub>2</sub>, 0.1% (w/v) BSA and no detergent. We determined the K<sub>m</sub> value of 191 ± 31 μM towards egg yolk LPC. We validated the preparation further by showing that the end-product LPA (Suppl. Fig. S7) or the artificial substrate pNP-TMP (*p*-nitrophenyl thymidine 5'-monophosphate) (Suppl. Fig. S8) did not inhibit ewATX-catalyzed LPC hydrolysis. In contrast, LPC totally prevented ewATX-mediated hydrolysis of pNP-TMP (Suppl. Fig. S9). Collectively these experiments verified that ewATX activity assays are a reliable tool for initial discovery of ATX inhibitors.

We used 100 μM LPC in all inhibitor screening assays and first tested the behavior of HA155, PF8380 and S32826 as reference inhibitors (Fig. 2). HA155 and PF8380 displayed 100% and 84.4% of ewATX inhibition at 10 μM concentration, respectively. Interestingly, S32826 displayed only partial inhibition (35.4%) in ewATX assay when tested at 10 μM concentration. As our docking results identified 26 potential compounds, we obtained these compounds and tested them using ewATX activity assay. We noticed that two of the compounds displaying ATX inhibitory activity shared a similar 2,4-dihydropyrano[2,3-*c*]pyrazole scaffold (Fig. 4). Compound **1** exhibited ~55% inhibition of ewATX, whereas compound **2** displayed ~20% inhibition when tested at 10 μM concentration. Utilizing Canvas (“Canvas,” 2014), we confirmed that the two compounds did not belong to pan-assay interfering compounds PAINS (Baell and Holloway, 2010), which was indeed later confirmed with the best derivatives in the series (data not shown).

### 3.3. Optimization of the 2,4-dihydropyrano[2,3-*c*]pyrazole scaffold

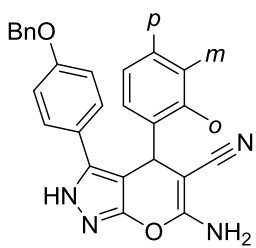
As the first set of active compounds displayed a potential scaffold for ATX inhibition, we pursued a search for commercially available compounds with the identical 2,4-dihydropyrano[2,3-*c*]pyrazole scaffold. We conducted IFD (Farid et al., 2006; “Induced Fit Docking,” 2015; Sherman et al., 2006a, 2006b) for the available compounds and according to the IFD results, a total of 27 compounds were purchased and tested for ewATX inhibitory activity. From this series, compounds **3**, **4**, **5**, and **6** inhibited ewATX (Table 1). Clearly, the most potent compound from this set was compound **3**, displaying 94.3% inhibition of ewATX at 10  $\mu$ M concentration. We noticed that a phenyl ring directly attached in the R1 position was crucial for the activity. The tested inactive 2,4-dihydropyrano[2,3-*c*]pyrazoles are listed in Suppl. Table S1.

**Table 1.** The most active 2,4-dihydropyrano[2,3-*c*]pyrazoles from series 2.

compd	ewATX inhibition (%) at 10 $\mu$ M $\pm$ SEM		
		R <sup>1</sup>	R <sup>2</sup>
<b>3</b>	94.3 $\pm$ 1.00		
<b>4</b>	16.0 $\pm$ 3.40		
<b>5</b>	42.0 $\pm$ 1.45		
<b>6</b>	27.7 $\pm$ 0.40		

Next, we pursued with the compound **3** scaffold. We began by exploring the chemical space in the R2 aromatic ring by testing various substituents that were commercially available (Table 2).

**Table 2.** R2 substituent effect on biological activity.

compd	ewATX inhibition (%) at 10 $\mu$ M $\pm$ SEM			
		<i>o</i>	<i>m</i>	<i>p</i>
<b>3</b>	94.3 $\pm$ 1.00	H	Cl	Cl
<b>7</b>	14.7 $\pm$ 5.20	H	H	-OCH <sub>2</sub> CONH <sub>2</sub>
<b>8</b>	10.9 $\pm$ 2.05	H	H	F
<b>9</b>	31.7 $\pm$ 2.20	Cl	Cl	H
<b>10</b>	32.9 $\pm$ 0.60	Cl	H	Cl
<b>11</b>	0	H	H	-OPr
<b>12</b>	47.4 $\pm$ 0.50	H	H	-CF <sub>3</sub>
<b>13</b>	0	H	H	-O <sup>t</sup> Pr
<b>14</b>	65.0 $\pm$ 0.65	H	H	Br
<b>15</b>	57.2 $\pm$ 0.15	H	H	Cl
<b>16</b>	0	H	H	-OEt
<b>17</b>	3.8 $\pm$ 1.75	Cl	H	H

We noticed that relatively small electron withdrawing *m*- and *p*-substituents were crucial for the activity (**3**, **12**, **14**, **15**), whereas bulkier electron donating substituents in the *p*-position diminished activity (**7**, **11**, **13**, **16**).

Moreover, *o*-substitution diminished activity. We assume that the *o*-substitution (**9**, **10**, **17**) creates steric hindrance for the ring rotation, thereby forcing the ring and other substituents in the ring in suboptimal position. However, as none of the substituents improved the activity compared to the original compound **3**, we decided to retain R2 as 3'4'-dichlorophenyl. In addition to these compounds, we had already tested a *m*-OH derivative in series 2 and found it to be inactive (Suppl. Table S1).

Subsequently, we decided to modify the R1 (see Table 1) by synthesis, as reasonable derivatives for this position were not commercially available. According to our molecular modeling studies, mainly lipophilic residues should occur near this position. Furthermore, we had noticed in series 2 that a phenyl ring directly attached to pyrazole was required for activity (Table 1 and Suppl. Table S1). Therefore, to scan the spatial environment in R1 in the first synthesis set, we changed the position of the benzyloxy-substituent on the phenyl ring to *m*- and *o*-positions, and synthesized the original *p*-derivative as well (**18-20**) (Table 3). In addition, we also synthesized shorter *o*- *m*- and *p*-phenoxy derivatives (**21-23**).

With no improvement in the activity with the synthesized compounds in the first set, we continued pursuing with the spatial orientation in R1 of compound **19**. As molecular modeling results indicated additional space in the *p*-position of R1, we synthesized *p*-halogenated analogs (**24-25**). Accordingly, we observed 100% inhibition of ewATX at 10  $\mu$ M concentration with these *p*-halogenated compounds, (*S*)-**24** and (*S*)-**25** (IC<sub>50</sub>-values of 149 nM and 87 nM, respectively). In addition, we synthesized 1-phenylpyrazole derivatives (**26-28**), which obtained promising docking poses, and tested the inhibitor activity of this series of compounds against ewATX preparation (Table 3).

#### 3.4. Chemical synthesis of novel 2,4-dihydropyrano[2,3-*c*]pyrazoles

The corresponding  $\beta$ -keto esters (Scheme 1) were synthesized from carboxylic acids (**1a-k**) by Masamune-Claisen type condensation (Brooks et al., 1979). Reaction of carboxylic acid (**1a-k**) with monomethyl magnesium malonate (**2a**) afforded  $\beta$ -keto ester (**3a-k**) which with hydrazine hydrate (1:1 mol) in refluxing ethanol afforded 1*H*-pyrazol-5(4*H*)-one (**4a-k**). The desired dihydropyrano[2,3-*c*]pyrazoles (**18-28**) we prepared in a three-component reaction (Lehmann et al., 2008) using 1*H*-pyrazol-5(4*H*)-one (**4a-k**), 3,4-dichlorobenzaldehyde (**5a**), and malononitrile (**6a**) (Scheme 1).

ACCEPTED MANUSCRIPT

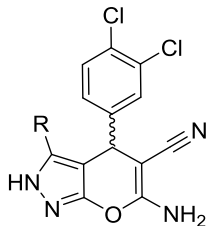
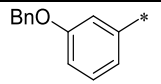
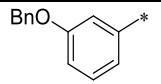
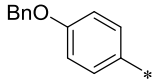
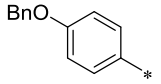
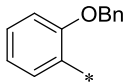
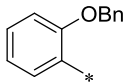
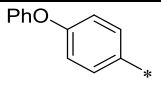
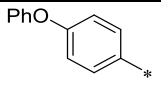
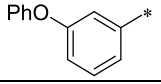
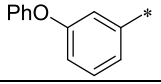
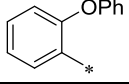
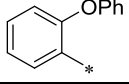
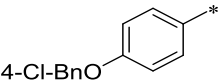
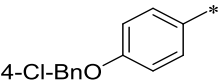
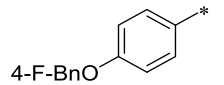
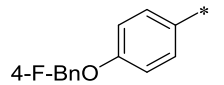
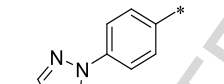
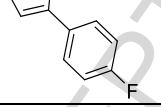
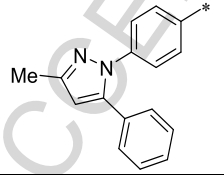
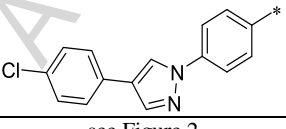


### 3.5. Validation of human ATX inhibition

Next, as our initial activity data were obtained using the ewATX preparation, we validated our hit compounds using purified recombinant hATX with LPC as the substrate. Importantly, the hATX inhibition data were found to closely match with those obtained using the ewATX preparation (Table 3), suggesting further that the ewATX activity assay indeed represents a valid approach in the initial discovery of ATX inhibitors. Only four of the tested compounds displayed >10% difference in the degree of inhibition between ewATX and hATX when tested at 10  $\mu$ M concentration. Excluding these outliers, the active compounds displayed only minor difference in the extent of ewATX and hATX inhibition (average of 2.68%). The reference inhibitor HA155 exhibited similar level of hATX inhibition as with ewATX; its potency was similar in both preparations ( $IC_{50}$ -values of 15 nM and 13 nM, respectively). The reference inhibitor PF8380 exhibited similar level of inhibition in both ewATX and hATX at 10  $\mu$ M, however, its potency was clearly lower in the ewATX preparation (Table 3; Suppl. Fig. S13a-b). We cannot currently explain this differential outcome.

The reference inhibitor S32826 which displayed only modest inhibition of ewATX at 10  $\mu$ M, showed better inhibition with hATX (70.7%). Furthermore, we noticed that S32826 did not fully inhibit hATX or ewATX as ~30% and ~70% residual activity remained even at 100  $\mu$ M inhibitor concentration. (Suppl. Fig. S13a-b). However, S32826 inhibited fully the hydrolysis of the artificial substrate pNP-TMP, and with low nanomolar potency (Suppl. Fig. S13c-d). These findings can be explained, as S32826 was originally reported as a low nanomolar ATX inhibitor using only an artificial substrate in the inhibition assay, and not LPC (Ferry et al., 2008). This differential outcome suggests that while S32826 fully competes with pNP-TMP in the active site, it can only partially block access of the natural substrate LPC to this site.

**Table 3.** Synthesized 2,4-dihydropyrano[2,3-*c*]pyrazole derivatives and reference compounds (HA155, PF8380, S32826), and their activities in ewATX and hATX assays with LPC as the substrate.

compd		ewATX inhibition (%) at 10 $\mu$ M $\pm$ SEM	hATX inhibition (%) at 10 $\mu$ M $\pm$ SEM	ewATX IC <sub>50</sub> (nM) $\pm$ SEM	hATX IC <sub>50</sub> (nM) $\pm$ SEM
( <i>R</i> )-18		31.1 $\pm$ 1.05	0	nd	
( <i>S</i> )-18		56.6 $\pm$ 0.10	59.5 $\pm$ 0.60	2142 $\pm$ 178	
( <i>R</i> )-19		0	0	nd	
( <i>S</i> )-19		94.7 $\pm$ 0.65	92.9 $\pm$ 0.30	166 $\pm$ 15 <sup>a</sup>	
( <i>R</i> )-20		14.1 $\pm$ 1.40	0	nd	
( <i>S</i> )-20		72.1 $\pm$ 1.80	70.8 $\pm$ 1.00	1963 $\pm$ 151	
( <i>R</i> )-21		0	0	nd	
( <i>S</i> )-21		79.6 $\pm$ 0.60	75.1 $\pm$ 0.30	335 $\pm$ 47	
( <i>R</i> )-22		0	0	nd	
( <i>S</i> )-22		77.9 $\pm$ 0.80	72.8 $\pm$ 0.20	954 $\pm$ 55	
( <i>R</i> )-23		4.7 $\pm$ 2.40	0	nd	
( <i>S</i> )-23		72.7 $\pm$ 2.90	67.7 $\pm$ 0.40	1929 $\pm$ 160	
( <i>R</i> )-24		0	0	nd	
( <i>S</i> )-24		100.0 $\pm$ 0.25	97.3 $\pm$ 0.60	149 $\pm$ 21 <sup>a</sup>	209 $\pm$ 32 <sup>a</sup>
( <i>R</i> )-25		0	0	nd	
( <i>S</i> )-25		100.0 $\pm$ 2.05	99.3 $\pm$ 0.55	87 $\pm$ 12 <sup>a</sup>	134 $\pm$ 16 <sup>a</sup>
( <i>rac</i> )-26		32.8 $\pm$ 1.10	27.7 $\pm$ 0.80		nd
27A (enantiomer A)		17.0 $\pm$ 4.30	16.3 $\pm$ 1.85		nd
27B (enantiomer B)		53.2 $\pm$ 0.35	51.6 $\pm$ 0.55		nd
( <i>rac</i> )-28		85.7 $\pm$ 0.20	69.0 $\pm$ 3.05	2120 $\pm$ 1051	2566 $\pm$ 1478
HA155	see Figure 2	100.0 $\pm$ 3.9	96.9 $\pm$ 3.10	13 $\pm$ 1 <sup>a</sup>	15 $\pm$ 1 <sup>a</sup>
PF8380	see Figure 2	84.4 $\pm$ 1.8	85.0 $\pm$ 6.0	951 $\pm$ 200 <sup>a</sup>	70 $\pm$ 20 <sup>a</sup>
S32826	see Figure 2	35.4 $\pm$ 19.9	70.7 $\pm$ 13.8	115 $\pm$ 75 <sup>a</sup>	94 $\pm$ 17 <sup>a</sup>

<sup>a</sup>The dose response curves for the reference inhibitors and compounds (*S*)-19, 24 & 25 are shown in Suppl. Fig. S13; nd = not determined

### 3.6. Only *S*-enantiomer of 2,4-dihydropyrano[2,3-*c*]pyrazoles exhibit ATX inhibition

Compounds with the 2,4-dihydropyrano[2,3-*c*]pyrazole scaffold are chiral and, interestingly, the docking made a clear distinction between the enantiomers; we observed only *S*-enantiomer in our best docking poses. As we did not observe any *R*-enantiomers of these compounds in our final results, we utilized QM-polarized ligand docking (Cho et al., 2005; “QM-Polarized Ligand Docking protocol,” 2015) for both enantiomers to gain deeper insight into their differences. The docking proposed totally distinct binding modes for the enantiomers, and they differed significantly in their docking score as well. For *S*- and *R*-enantiomers, XP docking scores for compound **1** were -16.124 and -9.219, and for compound **2** -16.454 and -10.081, respectively. Moreover, the poses with *R*-enantiomers were not converged. Hence, the docking studies clearly suggested that the enantiomers likely differed in their biological activity.

We set up to validate this hypothesis and separated the enantiomers for structural analysis and activity determination. The racemic 2,4-dihydropyrano[2,3-*c*]pyrazoles **18-25** and **27** were separated into their pure enantiomers using a chiral chromatography (see S24 in Suppl. Information). To determine the absolute configuration, the separated enantiomers were subjected to single crystal X-ray analysis, which revealed the absolute configuration of the first-eluted enantiomer of **19** to be (*R*), second-eluted enantiomer of **18** to be (*S*), second-eluted enantiomer of **23** to be (*S*), and second-eluted enantiomer of **25** to be (*S*) (see Fig. 5; Experimental Section; and Suppl. Fig. S10). As the configuration is expected to remain the same for other enantiomers, we concluded by analogy that the first-eluted isomers represent the *R*-configuration, and the second-eluted isomer represents the *S*-configuration.

Interestingly, activity assays using the separated enantiomers indicated ATX inhibition only with the *S*-enantiomers, as predicted correctly by the molecular docking (Table 3). The *S*-enantiomer of compound **19** inhibited ATX with an IC<sub>50</sub> value of 166 nM, whereas the *R*-enantiomer displayed practically no inhibition of hATX or ewATX when tested at 10 μM concentration. On the whole, we observed that with all active compounds with separated enantiomers, the *S*-enantiomer was the only active isomer. Worth noting, enantiomers of compounds **26** and **28** could not be separated due to their extremely low solubility.

From the synthesized series, compound (*S*)-**25** displayed the highest potency of inhibition (IC<sub>50</sub>-values of 87 and 134 nM for ewATX and hATX, respectively) (Table 3 and Suppl. Fig. S13a-b).

### 3.7. Putative binding mode of 2,4-dihydropyrano[2,3-*c*]pyrazoles

According to molecular docking results, *S*-enantiomers of 2,4-dihydropyrano[2,3-*c*]pyrazoles obtain similar binding modes. All the best scoring docking poses of *S*-enantiomer 2,4-dihydropyrano[2,3-*c*]pyrazoles with Glide, QM-polarized ligand docking and IFD converged nicely to the same orientation (Suppl. Fig. S11). Here, we use the most potent compound [(*S*)-**25**] as an example of the putative binding interactions of a 2,4-dihydropyrano[2,3-*c*]pyrazoles with ATX. To note, hATX amino acid numbering is used throughout the section.

From the 2,4-dihydropyrano[2,3-*c*]pyrazole scaffold, compound forms a stacking interaction with Y307, which lies on the bottom of the cavity's entrance (Fig. 6). The nitrogens from the pyrazole ring form a hydrogen bond with F274 backbone oxygen and W276 backbone NH. The oxygen of the ring forms a hydrogen bond to a bridging water molecule, which forms interaction to backbone oxygen of W276. The amino group, which orients towards solvent, is either able to interact with the solvent or it may form a hydrogen bond with E309. The cyano group is capable of interacting with R245. The phenyl in R2 has an edge-to-face  $\pi$ - $\pi$  interaction with F211, and additionally with F275 in most of the docking poses. As the F274 and F275 sidechains are flexible (see Suppl. Fig. S11), we were not able to confirm which of these orientations they prefer. However, the backbone hydrogen bonding pattern remains similar with these residues, regardless of the side chain orientation.

Presumably, halogens in R1 and R2 may not only aid the compound occupy the cavity firmly, but they may have an effect in optimizing the putative  $\pi$ - $\pi$  interactions with F211, F275 and F274. Indeed, the compound activity changed based on the characteristics of *p*-substituent in R2;  $-\text{CF}_3 < -\text{Cl} < -\text{Br}$  (Table 2). These substituents have an effect in the  $\pi$ -electrons in the ligand's R2-ring, and may accordingly strengthen or weaken the  $\pi$ - $\pi$  interaction with the protein.

Mainly lipophilic residues I168, L217, L260, W261, A305 and M513 lay on the end of the pocket (Suppl. Fig. S12), and cavity fitting lipophilic characteristic owing R1 exhibit biological activity. Moreover, the distal phenyl ring in R1 might establish  $\pi$ - $\pi$  interactions, with W261 or F274.

To further support these interactions, the published ATX crystal structures with bound inhibitors display similar features in their interactions with ATX. For example, in the 5L0E<sup>[56]</sup> structure, similar hydrogen bonding pattern with F274 and W276 exist. In addition, there is a  $\pi$ - $\pi$  stacking interaction with Y307, and F274 and F275 may form  $\pi$ - $\pi$  interactions with the inhibitor. Interestingly, especially the hydrogen bond with W276 and  $\pi$ - $\pi$

interaction with F275 seems to be crucial in the inhibitor binding. W276 hydrogen bond exist in 5L0K (Jones et al., 2016) (PF8380), 5L0B (Jones et al., 2016), 5L0E (Jones et al., 2016), 4ZGA (Stein et al., 2015), 4ZG6 (Stein et al., 2015), 3WAV (Kawaguchi et al., 2013), 3WAW (Kawaguchi et al., 2013), 3WAX (Kawaguchi et al., 2013) and 3WAY (Kawaguchi et al., 2013) structures, whereas  $\pi$ - $\pi$  interaction with F275 can be observed in 5L0B (Jones et al., 2016), 5L0E (Jones et al., 2016), 4ZG7 (Stein et al., 2015), 4ZG9 (Stein et al., 2015), 4ZGA (Stein et al., 2015), 3WAW (Kawaguchi et al., 2013) and 3WAX (Kawaguchi et al., 2013) structures.

To further support the idea that these compounds do not interact with the catalytic site, we used the artificial substrate pNP-TMP in ATX activity assay with the outcome that the most potent compounds with 2,4-dihydropyrano[2,3-*c*]pyrazole scaffold which were able to completely inhibit LPC hydrolysis, were unable to inhibit fully pNP-TMP hydrolysis (Suppl. Figure S13c-d). Compound (*S*)-**19**, (*S*)-**24** and (*S*)-**25** inhibited pNP-TMP hydrolysis by 10% to 20% at 100 nM, whereas HA155, PF8380 and S32826 which all bind to the active site, inhibited fully the pNP-TMP hydrolysis at the same concentration.

Collectively these results support the notion that compounds with this scaffold do not directly interact with the catalytic site but instead by binding to the lipophilic pocket, disturb proper orientation of the LPC's lipophilic tail to the pocket, thereby blocking efficient LPC hydrolysis. Moreover, the difference in the activity of enantiomers (Table 3) supports this binding mode. As inhibition of ATX is achieved only with *S*-enantiomers and the *R*-enantiomer is not able to achieve this type of binding.

### 3.8. Hydration site analysis

To gain more insight into the binding pocket properties and to understand more profoundly the binding mode of 2,4-dihydropyrano[2,3-*c*]pyrazole derivatives' to ATX, we conducted a hydration site analysis with WaterMap (Abel et al., 2008; "WaterMap," 2015; Young et al., 2007). We used the 3WAX structure with the boronic acid inhibitor for the WaterMap simulation. Interestingly, this analysis revealed that two de-wetted regions existed in the binding site. One in the lipophilic pocket and another in the lipophilic tunnel entrance (Fig. 7). These de-wetted regions are energetically highly unfavorable for water molecules to bind (penalty of 6-8 kcal/mol), leaving a vacuum in the sites, allowing high-energy gain for inhibitors which occupy these sites. In fact, the compounds which display the highest activity of the 2,4-dihydropyrano[2,3-*c*]pyrazole series, are presumably occupying both of these sites. In addition, the analysis revealed that high-energy waters ( $\Delta G > 3$  kcal/mol) within 4 Å from the

crystallized ligand, exist around the dichlorophenyl and thiazol rings, and interestingly, on top of the carboxyl-group, which forms a hydrogen bond to W276 (Suppl. Fig. S14). According to our docking results, this hydrogen bond acceptor position is also occupied by 2,4-dihydropyrano[2,3-*c*]pyrazoles.

### 3.9. Assessment of compound (*S*)-**25** in Melanoma Cell Motility and its inhibition.

To verify our most potent compound's ability to affect in ATX-mediated signaling in a cell-based assay, we conducted a melanoma A2058 cell migration assay (Saunders et al., 2008). Cell migration was stimulated by inclusion of hATX and LPC or LPA to the lower chamber. The solvent, 0.1% (v/v) DMSO, had no effect on cell migration. The experimental treatment having 50 nM hATX with 50  $\mu$ M LPC, or 150 nM of LPA alone stimulated A2058 melanoma cell migration by 2 to 2.5-fold as compared to the basal condition (Fig. 8). Our most potent compound [(*S*)-**25**] and the reference inhibitor HA155 were tested at 1  $\mu$ M concentration and both compounds effectively inhibited migration evoked by ATX in the presence of LPC (Fig. 8b). Direct effects of LPA receptors or downstream signalling mediating cell migration were not evident, as (*S*)-**25** had no effect on LPA-evoked migration. In contrast, HA155 inhibited also LPA-induced cell migration in a statistically significant manner ( $p \leq 0.05$ ) suggesting that this compound may have off-targets downstream of ATX.

## 4. Conclusions

Using mATX crystal structure in virtual screening and validated ewATX preparation in the preliminary phase of inhibitor screening, we have identified a novel ATX inhibitor (*S*)-**25** that also inhibits hATX with an  $IC_{50}$ -value of 134 nM. We further validated (*S*)-**25** in melanoma cell migration assays, where the compound blocked ATX-mediated cell migration with no observed effect on LPA receptors or downstream signaling mediating cell migration. The 2,4-dihydropyrano[2,3-*c*]pyrazoles represent a totally different type of inhibitor as compared to the traditional ATX inhibitors, as they most likely bind to the lipophilic pocket instead of the catalytic site. Interestingly, the molecular modeling was able to clearly distinguish the enantiomers of 2,4-dihydropyrano[2,3-*c*]pyrazoles, predicting correctly the biologically active enantiomer. Worth noting, a compound with the similar

2,4-dihydropyrano[2,3-*c*]pyrazole scaffold has been previously disclosed, although not further exploited, in HTS of ATX inhibitors (Albers et al., 2010).

Moreover, we have validated the ewATX screening assay as a convenient and cost-effective tool in the initial discovery of ATX inhibitors. With few notable exceptions, the ewATX assay faithfully reflected results obtained with hATX preparation. The strength of this assay lies in its affordability, as an egg white separated from a single egg provided sufficient amounts of material for the entire screening phase of the present study. However, as with any biological material, batch-to-batch variation can be expected also with ewATX preparations. Therefore, initial validation as provided for the presently used preparation (Suppl. Information S8-S12) should be done for every new batch.

We noticed that the reference inhibitor S32826 was not effectively inhibiting LPC hydrolysis although it performed well in assays with the artificial substrate pNP-TMP. This can be taken as a cautionary example of using an unnatural substrate in the screening assay, generating the possibility for false positive results. In addition, the use of natural substrate enabled us to identify inhibitors which leave the active site unhindered or do not compete with the substrate or both. On the other hand, with the artificial substrate, we were able to provide additional evidence that 2,4-dihydropyrano[2,3-*c*]pyrazoles leave the enzyme's active site unhindered, as inhibition of pNP-TMP hydrolysis was minor with these compounds.

Our data suggested that the novel 2,4-dihydropyrano[2,3-*c*]pyrazoles likely inhibit ATX by binding to the lipophilic pocket instead of the enzyme's active-site. Unfortunately, as the pocket of ATX is highly-lipophilic, it drives the inhibitors which target this site to have high logP values. To overcome this phenomenon, new strategies need to be considered when aiming at targeting this pocket. One potential approach could be to find all plausible hydrogen bond contacts within the pocket to decrease the logP values of the inhibitors. Especially S170, which lies deep in the pocket, could be an attractive target to establish hydrogen bond in order to obtain inhibitors with lower logP values. Another possibility would be utilizing the open solvent interface of the binding pocket. For instance, attaching a hydrophilic moiety towards the solvent phase from the inhibitor, could solve the high logP issue.

In conclusion, this study has characterized novel type of ATX inhibitors showing nanomolar potency and targeting the lipophilic pocket, expanding the pharmacological toolkit to manipulate ATX activity in settings where inhibition of ATX activity would be desirable.

### Conflict of interest

The authors declare no competing financial interest.

### Abbreviations

HTVS, high-throughput virtual screening; SP, standard precision; XP, extra precision; IFD, Induced Fit Docking; LPC, lysophosphatidylcholine; LPA, lysophosphatidic acid ; ewATX, hen egg white Autotaxin; mATX, mouse Autotaxin; hATX, human Autotaxin; lysoPLD, lysophospholipase D; pNP-TMP, (*p*-nitrophenyl thymidine 5'-monophosphate);

### Acknowledgements

We would like to thank Taina Vihavainen and Tiina Koivunen for technical assistance, and the Finland's CSC - IT Center for Science Ltd. for the computational resources. This study was supported by the Academy of Finland (grant 276509 to AP; grant 278212 to JTL) and Biocenter Finland/DDCB (TL).

### Appendix A. Supplementary data

Appendix A. Supplementary material

### Appendix A. Supplementary data

Supplementary information contains structural comparison of mATX, ewATX and hATX, validation and optimization of ewATX screening assay, crystal structures of compounds **18**, **19** and **23**, IFD-poses of (*S*)-**19**, closer look of lipophilic pocket residues nearby compound (*S*)-**25**, dose-response curves for selected compounds, high-energy hydration sites within the binding pocket, additional synthesis and spectroscopic analysis data, purity data of compound crystallization data, NMR data for purchased compounds.



## References

- Abel, R., Young, T., Farid, R., Berne, B.J., Friesner, R.A., 2008. The role of the active site solvent in the thermodynamics of factor Xa-ligand binding. *J. Am. Chem. Soc.* 130, 2817–2831. doi:10.1021/ja0771033
- Albers, H.M.H.G., Van Meeteren, L. a., Egan, D. a., Van Tilburg, E.W., Moolenaar, W.H., Ovaa, H., 2010. Discovery and optimization of boronic acid based inhibitors of Autotaxin. *J. Med. Chem.* 53, 4958–4967. doi:10.1021/jm1005012
- Aoki, J., Taira, A., Takanezawa, Y., Kishi, Y., Hama, K., Kishimoto, T., Mizuno, K., Saku, K., Taguchi, R., Arai, H., 2002. Serum lysophosphatidic acid is produced through diverse phospholipase pathways. *J. Biol. Chem.* 277, 48737–48744. doi:10.1074/jbc.M206812200
- APEX2, 2010. APEX2 - Software Suite for Crystallographic Programs, Bruker AXS, Inc.: Madison, WI, USA
- Baell, J.B., Holloway, G.A., 2010. New substructure filters for removal of pan assay interference compounds (PAINS) from screening libraries and for their exclusion in bioassays. *J. Med. Chem.* 53, 2719–2740. doi:10.1021/jm901137j
- Banerjee, S., Norman, D.D., Lee, S.C., Parrill, A.L., Pham, T.C.T., Baker, D.L., Tigyi, G.J., Miller, D.D., 2017. Highly Potent Non-Carboxylic Acid Autotaxin Inhibitors Reduce Melanoma Metastasis and Chemotherapeutic Resistance of Breast Cancer Stem Cells. *J. Med. Chem.* 60, 1309–1324. doi:10.1021/acs.jmedchem.6b01270
- Banks, J.L., Beard, H.S., Cao, Y., Cho, A.E., Damm, W., Farid, R., Felts, A.K., Halgren, T.A., Mainz, D.T., Maple, J.R., Murphy, R., Philipp, D.M., Repasky, M.P., Zhang, L.Y., Berne, B.J., Friesner, R.A., Gallicchio, E., Levy, R.M., 2005. Integrated Modeling Program, Applied Chemical Theory (IMPACT). *J. Comput. Chem.* 26, 1752–1780. doi:10.1002/jcc.20292
- Bochevarov, A.D., Harder, E., Hughes, T.F., Greenwood, J.R., Braden, D.A., Philipp, D.M., Rinaldo, D., Halls, M.D., Zhang, J., Friesner, R.A., 2013. Jaguar: A high-performance quantum chemistry software program with strengths in life and materials sciences. *Int. J. Quantum Chem.* 113, 2110–2142. doi:10.1002/qua.24481
- Brindley, D.N., Lin, F.T., Tigyi, G.J., 2013. Role of the autotaxin-lysophosphatidate axis in cancer resistance to chemotherapy and radiotherapy. *Biochim. Biophys. Acta - Mol. Cell Biol. Lipids* 1831, 74–85. doi:10.1016/j.bbali.2012.08.015
- Brooks, D.W., Lu, L.D., Masamune, S., 1979. No Title. *Angew. Chem. Int. Ed. Engl.* 72–74.
- Canvas, 2014. Canvas, version 2.1, Schrödinger, LLC, New York, NY.
- Castagna, D., Budd, D.C., MacDonald, S.J.F., Jamieson, C., Watson, A.J.B., 2016. Development of Autotaxin Inhibitors: An Overview of the Patent and Primary Literature. *J. Med. Chem.* 59, 5604–5621. doi:10.1021/acs.jmedchem.5b01599
- ChemBridge Corporation [WWW Document], 2014. URL <http://www.chembridge.com> (accessed 8.15.14).
- Cho, A.E., Guallar, V., Berne, B.J., Friesner, R., 2005. Importance of accurate charges in molecular docking: Quantum Mechanical/Molecular Mechanical (QM/MM) approach. *J. Comput. Chem.* 26, 915–931. doi:10.1002/jcc.20222
- COSMIC [WWW Document], 2016. Wellcome Trust Sanger Institute The Catalogue Of Somatic Mutations In Cancer (COSMIC v. 78). <http://cancer.sanger.ac.uk/cosmic/> (accessed 9/27, 2016).
- Enamine Ltd [WWW Document], 2014. Enamine Ltd <http://www.enamine.net> (accessed 2, 2014).
- Epik, 2014. Epik, version 2.9, Schrödinger, LLC, New York, NY.
- Farid, R., Day, T., Friesner, R.A., Pearlstein, R.A., 2006. New insights about HERG blockade obtained from protein modeling, potential energy mapping, and docking studies. *Bioorganic Med. Chem.* 14, 3160–3173. doi:10.1016/j.bmc.2005.12.032
- Farrugia, L.J., 2012. WinGX and ORTEP for Windows: An update. *J. Appl. Crystallogr.* 45, 849–854.

doi:10.1107/S0021889812029111

- Fells, J.I., Lee, S.C., Fujiwara, Y., Norman, D.D., Lim, K.G., Tsukahara, R., Liu, J., Patil, R., Miller, D.D., Kirby, R.J., Nelson, S., Seibel, W., Papoian, R., Parrill, A.L., Baker, D.L., Bittman, R., Tigyi, G., 2013. Hits of a high-throughput screen identify the hydrophobic pocket of autotaxin/lysophospholipase D as an inhibitory surface. *Mol. Pharmacol.* 84, 415–424. doi:10.1124/mol.113.087080
- Ferry, G., Moulharat, N., Pradere, J.P., Desos, P., Try, A., Genton, A., Giganti, A., Beucher-Gaudin, M., Lonchamp, M., Bertrand, M., Saulnier-Blache, J.S., Tucker, G.C., Cordi, A., Boutin, J.A., 2008. S32826, a nanomolar inhibitor of autotaxin: discovery, synthesis and applications as a pharmacological tool. *J. Pharmacol. Exp. Ther.* 327, 809–819. doi:10.1124/jpet.108.141911
- FIMM [WWW Document], 2007. Institute for Molecular Medicine Finland (FIMM) <http://www.fimm.fi> (accessed 11, 2007).
- Fotopoulou, S., Oikonomou, N., Grigorieva, E., Nikitopoulou, I., Paparountas, T., Thanassopoulou, A., Zhao, Z., Xu, Y., Kontoyiannis, D.L., Remboutsika, E., Aidinis, V., 2010. ATX expression and LPA signalling are vital for the development of the nervous system. *Dev. Biol.* 339, 451–464. doi:10.1016/j.ydbio.2010.01.007
- Friesner, R.A., Banks, J.L., Murphy, R.B., Halgren, T.A., Klicic, J.J., Mainz, D.T., Repasky, M.P., Knoll, E.H., Shelley, M., Perry, J.K., Shaw, D.E., Francis, P., Shenkin, P.S., 2004. Glide: A New Approach for Rapid, Accurate Docking and Scoring. 1. Method and Assessment of Docking Accuracy. *J. Med. Chem.* 47, 1739–1749. doi:10.1021/jm0306430
- Friesner, R.A., Murphy, R.B., Repasky, M.P., Frye, L.L., Greenwood, J.R., Halgren, T.A., Sanschagrin, P.C., Mainz, D.T., 2006. Extra precision glide: Docking and scoring incorporating a model of hydrophobic enclosure for protein-ligand complexes. *J. Med. Chem.* 49, 6177–6196. doi:10.1021/jm051256o
- Fukushima, N., Weiner, J. a, Kaushal, D., Contos, J.J. a, Rehen, S.K., Kingsbury, M. a, Kim, K.Y., Chun, J., 2002. Lysophosphatidic acid influences the morphology and motility of young, postmitotic cortical neurons. *Mol. Cell. Neurosci.* 20, 271–282. doi:10.1006/mcne.2002.1123
- Galapagos NV [WWW Document], 2000. . Study to Assess Safety, Tolerability, Pharmacokinetic. Pharmacodyn. Prop. GLPG1690. URL <http://clinicaltrials.gov/show/NCT02738801> (accessed 9.29.16).
- Gierse, J., Thorarensen, A., Beltey, K., Bradshaw-pierce, E., Cortes-burgos, L., Hall, T., Johnston, A., Murphy, M., Nemirovskiy, O., Ogawa, S., Pegg, L., Pelc, M., Prinsen, M., Schnute, M., Wendling, J., Wene, S., Weinberg, R., Wittwer, A., Zweifel, B., Masferrer, J., 2010. A Novel Autotaxin Inhibitor Reduces Lysophosphatidic Acid Levels in Plasma and the Site of Inflammation. *J. Pharmacol. Exp. Ther.* 1, 310–317. doi:10.1124/jpet.110.165845.
- Glide, 2014. Small-Molecule Drug Discovery Suite 2014-3 Glide, version 6.4, Schrödinger, LLC, New York, NY.
- Greenwood, J.R., Calkins, D., Sullivan, A.P., Shelley, J.C., 2010. Towards the comprehensive, rapid, and accurate prediction of the favorable tautomeric states of drug-like molecules in aqueous solution. *J. Comput. Aided. Mol. Des.* 24, 591–604. doi:10.1007/s10822-010-9349-1
- Halgren, T.A., Murphy, R.B., Friesner, R.A., Beard, H.S., Frye, L.L., Pollard, W.T., Banks, J.L., 2004. Glide: A New Approach for Rapid, Accurate Docking and Scoring. 2. Enrichment Factors in Database Screening. *J. Med. Chem.* 47, 1750–1759. doi:10.1021/jm030644s
- Harder, E., Damm, W., Maple, J., Wu, C., Reboul, M., Xiang, J.Y., Wang, L., Lupyan, D., Dahlgren, M.K., Knight, J.L., Kaus, J.W., Cerutti, D.S., Krilov, G., Jorgensen, W.L., Abel, R., Friesner, R.A., 2016. OPLS3: A Force Field Providing Broad Coverage of Drug-like Small Molecules and Proteins. *J. Chem. Theory Comput.* 12, 281–296. doi:10.1021/acs.jctc.5b00864
- Hausmann, J., Kamtekar, S., Christodoulou, E., Day, J.E., Wu, T., Fulkerson, Z., Albers, H.M.H.G., van Meeteren, L.A., Houben, A.J.S., van Zeijl, L., Jansen, S., Andries, M., Hall, T., Pegg, L.E., Benson, T.E., Kasiem, M., Harlos, K., Kooi, C.W. Vander, Smyth, S.S., Ovaa, H., Bollen, M., Morris, A.J., Moolenaar, W.H., Perrakis, A., 2011. Structural basis of substrate discrimination and integrin binding by autotaxin. *Nat Struct Mol Biol* 18, 198–204. doi:10.1038/nsmb.1980

- Hooft, R.W.W., Straver, L.H., Spek, A.L., 2008. Determination of absolute structure using Bayesian statistics on Bijvoet differences. *J. Appl. Crystallogr.* 41, 96–103. doi:10.1107/S0021889807059870
- Houben, A.J.S., Moolenaar, W.H., 2011. Autotaxin and LPA receptor signaling in cancer. *Cancer Metastasis Rev.* 30, 557–565. doi:10.1007/s10555-011-9319-7
- Iftinca, M., Hamid, J., Chen, L., Varela, D., Tadayonnejad, R., Altier, C., Turner, R.W., Zamponi, G.W., 2007. Regulation of T-type calcium channels by Rho-associated kinase. *Nat. Neurosci.* 10, 854–860. doi:10.1038/nn1921
- Induced Fit Docking, 2015. Small-Molecule Drug Discovery Suite 2015-1 Schrödinger Suite 2015-1 Induced Fit Docking protocol; Glide version 6.6, Schrödinger, LLC, New York, NY; Prime version 3.9, Schrödinger, LLC, New York, NY.
- Jacobsen, J.A., Major Jourden, J.L., Miller, M.T., Cohen, S.M., 2010. To bind zinc or not to bind zinc: An examination of innovative approaches to improved metalloproteinase inhibition. *Biochim. Biophys. Acta - Mol. Cell Res.* 1803, 72–94. doi:10.1016/j.bbamcr.2009.08.006
- Jalink, K., Moolenaar, W.H., Van Duijn, B., 1993. Lysophosphatidic acid is a chemoattractant for *Dictyostelium discoideum* amoebae. *Proc. Natl. Acad. Sci. U. S. A.* 90, 1857–1861. doi:10.1073/pnas.90.5.1857
- Jones, S.B., Pfeifer, L.A., Bleisch, T.J., Beauchamp, T.J., Durbin, J.D., Klimkowski, V.J., Hughes, N.E., Rito, C.J., Dao, Y., Gruber, J.M., Bui, H., Chambers, M.G., Chandrasekhar, S., Lin, C., McCann, D.J., Mudra, D.R., Oskins, J.L., Swearingen, C.A., Thirunavukkarasu, K., Norman, B.H., 2016. Novel Autotaxin Inhibitors for the Treatment of Osteoarthritis Pain: Lead Optimization via Structure-Based Drug Design. *ACS Med. Chem. Lett.* 7, 857–861. doi:10.1021/acsmedchemlett.6b00207
- Kakugawa, S., Langton, P.F., Zebisch, M., Howell, S.A., Chang, T.-H., Liu, Y., Feizi, T., Bineva, G., O'Reilly, N., Snijders, A.P., Jones, E.Y., Vincent, J.-P., 2015. Notum deacylates Wnt proteins to suppress signalling activity. *Nature* 519, 187–192. doi:10.1038/nature14259
- Kato, K., Ikeda, H., Miyakawa, S., Futakawa, S., Nonaka, Y., Fujiwara, M., Okudaira, S., Kano, K., Aoki, J., Morita, J., Ishitani, R., Nishimasu, H., Nakamura, Y., Nureki, O., 2016. Structural basis for specific inhibition of Autotaxin by a DNA aptamer. *Nat. Struct. Mol. Biol.* 23, 395–401. doi:10.1038/nsmb.3200
- Katsifa, A., Kaffe, E., Nikolaidou-Katsaridou, N., Economides, A.N., Newbigging, S., McKerlie, C., Aidinis, V., 2015. The bulk of autotaxin activity is dispensable for adult mouse life. *PLoS One* 10, 1–14. doi:10.1371/journal.pone.0143083
- Kawaguchi, M., Okabe, T., Okudaira, S., Nishimasu, H., Ishitani, R., Kojima, H., Nureki, O., Aoki, J., Nagano, T., 2013. Screening and X-ray crystal structure-based optimization of autotaxin (ENPP2) inhibitors, using a newly developed fluorescence probe. *ACS Chem. Biol.* 8, 1713–1721. doi:10.1021/cb400150c
- Kihara, Y., Maceyka, M., Spiegel, S., Chun, J., 2014. Lysophospholipid receptor nomenclature review: IUPHAR Review 8. *Br. J. Pharmacol.* 171, 3575–3594. doi:10.1111/bph.12678
- Knowlden, S., Georas, S.N., 2014. The autotaxin-LPA axis emerges as a novel regulator of lymphocyte homing and inflammation. *J. Immunol.* 192, 851–857. doi:10.4049/jimmunol.1302831
- Leblanc, R., Lee, S.-C., David, M., Bordet, J.-C., Norman, D.D., Patil, R., Miller, D., Sahay, D., Ribeiro, J., Clezardin, P., Tigyi, G.J., Peyruchaud, O., 2014. Interaction of platelet-derived autotaxin with tumor integrin  $\alpha V\beta 3$  controls metastasis of breast cancer cells to bone. *Blood* 124, 3141–3150. doi:10.1182/blood-2014-04-568683
- Leblanc, R., Peyruchaud, O., 2015. New insights into the autotaxin/LPA axis in cancer development and metastasis. *Exp. Cell Res.* 333, 183–189. doi:10.1016/j.yexcr.2014.11.010
- Lee, S.J., No, Y.R., Dang, D.T., Dang, L.H., Yang, V.W., Shim, H., Yun, C.C., 2013. Regulation of hypoxia-inducible factor 1 $\alpha$  (HIF-1 $\alpha$ ) by lysophosphatidic acid is dependent on interplay between p53 and Krüppel-like factor 5. *J. Biol. Chem.* 288, 25244–25253. doi:10.1074/jbc.M113.489708
- Lehmann, F., Holm, M., Laufer, S., 2008. Three-component combinatorial synthesis of novel dihydropyrano[2,3-c]pyrazoles. *J. Comb. Chem.* 10, 364–7. doi:10.1021/cc800028m

- LigPrep, 2014. LigPrep, version 3.1, Schrödinger, LLC, New York, NY.
- Liu, S., Umez-Goto, M., Murph, M., Lu, Y., Liu, W., Zhang, F., Yu, S., Stephens, L.C., Cui, X., Murrow, G., Coombes, K., Muller, W., Hung, M.C., Perou, C.M., Lee, A. V., Fang, X., Mills, G.B., 2009. Expression of Autotaxin and Lysophosphatidic Acid Receptors Increases Mammary Tumorigenesis, Invasion, and Metastases. *Cancer Cell* 15, 539–550. doi:10.1016/j.ccr.2009.03.027
- Maestro, 2016. Schrödinger Release 2016-2 Maestro, version 10.6, Schrödinger, LLC, New York, NY.
- Maestro, 2015. Schrödinger Release 2015-1 Maestro, version 10.1, Schrödinger, LLC, New York, NY.
- Maestro, 2014. Schrödinger Release 2014-3 Maestro, version 9.9, Schrödinger, LLC, New York, NY.
- Maybridge [WWW Document], 2014. Maybridge, Thermo Fisher Scientific Inc. <http://www.maybridge.com> (accessed 11, 2014).
- Miller, L.M., Keune, W.J., Castagna, D., Young, L.C., Duffy, E.L., Potjewyd, F., Salgado-Polo, F., Garc??a, P.E., Semaan, D., Pritchard, J.M., Perrakis, A., MacDonald, S.J.F., Jamieson, C., Watson, A.J.B., 2017. Structure-activity relationships of small molecule autotaxin inhibitors with a discrete binding mode. *J. Med. Chem.* 60, 722–748. doi:10.1021/acs.jmedchem.6b01597
- Moolenaar, W.H., Houben, A.J.S., Lee, S.J., Van Meeteren, L.A., 2013. Autotaxin in embryonic development. *Biochim. Biophys. Acta - Mol. Cell Biol. Lipids* 1831, 13–19. doi:10.1016/j.bbalip.2012.09.013
- Moolenaar, W.H., Van Meeteren, L.A., Giepmans, B.N.G., 2004. The ins and outs of lysophosphatidic acid signaling. *BioEssays* 26, 870–881. doi:10.1002/bies.20081
- Morishige, J., Touchika, K., Tanaka, T., Satouchi, K., Fukuzawa, K., Tokumura, A., 2007. Production of bioactive lysophosphatidic acid by lysophospholipase D in hen egg white. *Biochim. Biophys. Acta - Mol. Cell Biol. Lipids* 1771, 491–499. doi:10.1016/j.bbalip.2007.01.005
- Muccioli, G.G., Labar, G., Lambert, D.M., 2008. CAY10499, a novel monoglyceride lipase inhibitor evidenced by an expeditious MGL assay. *Chembiochem* 9, 2704–2710. doi:10.1002/cbic.200800428
- Nakane, S., Tokumura, A., Waku, K., Sugiura, T., 2001. Hen egg yolk and white contain high amounts of lysophosphatidic acids, growth factor-like lipids: Distinct Molecular species compositions. *Lipids* 36, 413–419. doi:10.1007/s11745-001-0737-1
- Nam, S.W., Clair, T., Schiffmann, E., Liotta, L.A., Stracke, M.L., 2000. A sensitive screening assay for secreted motility-stimulating factors. *Cell Motil. Cytoskeleton* 46, 279–284. doi:10.1002/1097-0169(200008)46:4<279::AID-CM5>3.0.CO;2-P
- Ohata, A., Nakatani, S., Sugiyama, T., Morimoto, T., 2012. Patent WO/2012/005227.
- Pamuklar, Z., Federico, L., Liu, S., Umez-Goto, M., Dong, A., Panchatcharam, M., Fulerson, Z., Berdyshev, E., Natarajan, V., Fang, X., van Meeteren, L.A., Moolenaar, W.H., Mills, G.B., Morris, A.J., Smyth, S.S., 2009. Autotaxin/Lysopholipase D and lysophosphatidic acid regulate murine hemostasis and thrombosis. *J. Biol. Chem.* 284, 7385–7394. doi:10.1074/jbc.M807820200
- Protein Preparation Wizard, 2015. Schrödinger Suite 2015-3 Protein Preparation Wizard; Epik version 3.3, Schrödinger, LLC, New York, NY; Impact version 6.8, Schrödinger, LLC, New York, NY; Prime version 4.1, Schrödinger, LLC, New York, NY.
- PyMOL, 2016. The PyMOL Molecular Graphics System, Version 1.7.4 Schrödinger, LLC, New York, NY.
- QM-Polarized Ligand Docking protocol, 2015. Small-Molecule Drug Discovery Suite 2015-1: Schrödinger Suite 2015-1 QM-Polarized Ligand Docking protocol; Glide version 6.6, Schrödinger, LLC, New York, NY; Jaguar version 8.7, Schrödinger, LLC, New York, NY; QSite version 6.6, Schrödinger, LLC, New York, NY.
- Sastry, M.G., Adzhigirey, M., Day, T., Annabhimoju, R., Sherman, W., 2013. Protein and ligand preparation: Parameters, protocols, and influence on virtual screening enrichments. *J. Comput. Aided. Mol. Des.* 27,

221–234. doi:10.1007/s10822-013-9644-8

- Saunders, L.P., Ouellette, A., Bandle, R., Chang, W.C., Zhou, H., Misra, R.N., De La Cruz, E.M., Braddock, D.T., 2008. Identification of small-molecule inhibitors of autotaxin that inhibit melanoma cell migration and invasion. *Mol. Cancer Ther.* 7, 3352–62. doi:10.1158/1535-7163.MCT-08-0463
- Schrödinger Suite 2014-3 Protein Preparation Wizard, 2014; Epik version 2.9, Schrödinger, LLC, New York, NY; Impact version 6.4, Schrödinger, LLC, New York, NY; Prime version 3.7, Schrödinger, LLC, New York, NY.
- Shah, P., Cheasty, A., Foxton, C., Raynham, T., Farooq, M., Gutierrez, I.F., Lejeune, A., Pritchard, M., Turnbull, A., Pang, L., Owen, P., Boyd, S., Stowell, A., Jordan, A., Hamilton, N.M., Hitchin, J.R., Stockley, M., MacDonald, E., Quesada, M.J., Trivier, E., Skeete, J., Ovaa, H., Moolenaar, W.H., Ryder, H., 2016. Discovery of potent inhibitors of the lysophospholipase autotaxin. *Bioorganic Med. Chem. Lett.* 26, 5403–5410. doi:10.1016/j.bmcl.2016.10.036
- Sheldrick, G.M., 2015. Crystal structure refinement with SHELXL. *Acta Crystallogr. Sect. C Struct. Chem.* 71, 3–8. doi:10.1107/S2053229614024218
- Sheldrick, G.M., 2008. SADABS-2008/1 - Bruker AXS Area Detector Scaling and Absorption Correction.
- Shelley, J.C., Cholleti, A., Frye, L.L., Greenwood, J.R., Timlin, M.R., Uchimaya, M., 2007. Epik: A software program for pKa prediction and protonation state generation for drug-like molecules. *J. Comput. Aided. Mol. Des.* 21, 681–691. doi:10.1007/s10822-007-9133-z
- Sherman, W., Beard, H.S., Farid, R., 2006a. Use of an induced fit receptor structure in virtual screening. *Chem. Biol. Drug Des.* 67, 83–84. doi:10.1111/j.1747-0285.2005.00327.x
- Sherman, W., Day, T., Jacobson, M.P., Friesner, R.A., Farid, R., 2006b. Novel procedure for modeling ligand/receptor induced fit effects. *J. Med. Chem.* 49, 534–553. doi:10.1021/jm050540c
- Spek, A.L., 2013. PLATON, A Multipurpose Crystallographic Tool, 1.17 ; Utrecht University: Utrecht, The Netherlands.
- Stein, A.J., Bain, G., Prodanovich, P., Santini, A.M., Darlington, J., Stelzer, N.M.P., Sidhu, R.S., Schaub, J., Goulet, L., Lonergan, D., Calderon, I., Evans, J.F., Hutchinson, J.H., 2015. Structural Basis for Inhibition of Human Autotaxin by Four Potent Compounds with Distinct Modes of Binding. *Mol. Pharmacol.* 88, 982–992. doi:10.1124/mol.115.100404
- Tokumura, A., Iimori, M., Nishioka, Y., Kitahara, M., Sakashita, M., Tanaka, S., 1994. Lysophosphatidic acids induce proliferation of cultured vascular smooth muscle cells from rat aorta. *Am. J. Physiol. - Cell Physiol.* 267, C204–C210.
- Umezu-Goto, M., Kishi, Y., Taira, A., Hama, K., Dohmae, N., Takio, K., Yamori, T., Mills, G.B., Inoue, K., Aoki, J., Arai, H., 2002. Autotaxin has lysophospholipase D activity leading to tumor cell growth and motility by lysophosphatidic acid production. *J. Cell Biol.* 158, 227–233. doi:10.1083/jcb.200204026
- van Meeteren, L.A., Ruurs, P., Stortelers, C., Bouwman, P., van Rooijen, M.A., Pradere, J.P., Pettit, T.R., Wakelam, M.J.O., Saulnier-Blache, J.S., Mummery, C.L., Moolenaar, W.H., Jonkers, J., 2006. Autotaxin, a Secreted Lysophospholipase D, Is Essential for Blood Vessel Formation during Development. *Mol. Cell. Biol.* 26, 5015–5022. doi:10.1128/MCB.02419-05
- WaterMap, 2015. Schrödinger Release 2015-3: WaterMap, version 2.4, Schrödinger, LLC, New York, NY.
- Young, T., Abel, R., Kim, B., Berne, B.J., Friesner, R.A., 2007. Motifs for molecular recognition exploiting hydrophobic enclosure in protein–ligand binding. *Proc. Natl. Acad. Sci.* 104, 808–813. doi:10.1073/pnas.0610202104

**Figure 1.** ENPP2 gene amplification. Data from Copy Number Analysis (CONAN) of The Catalogue Of Somatic Mutations In Cancer (COSMIC v. 78).

**Figure 2.** Examples of reported ATX-inhibitors.

**Figure 3.** Virtual screening protocol. Four different libraries were prepared with LigPrep, and resulting molecules were docked with Glide with HTVS precision. Top scoring molecules were further docked with SP precision, and top scoring 1,000 molecules from SP results were further docked with XP. These XP results were filtered with Canvas using ALogP value, number of hydrogen bond acceptors (HBA) and hydrogen bond donors (HBD) as criteria. After filtering the results, best 250 molecules from each library were visually evaluated. Visual evaluation resulted in 89 molecules, which were clustered using 2D fingerprints. The representative molecules (67) from the clusters, were docked using IFD. Based on IFD results, visual evaluation resulted in final 26 molecules.

**Figure 4.** Structures of the hit compounds with 2,4-dihydropyrano[2,3-*c*]pyrazole scaffold

**Scheme 1.** General sequence for the preparation of 2,4-dihydropyrano[2,3-*c*]pyrazoles.

**Figure 5.** Crystal structure of (+)-(*S*)-isomer of compound **25** (CCDC:1526902).

**Figure 6.** An IFD-pose showing putative interactions of compound (*S*)-**25** (ball and stick, orange) with ATX. The 4-F-BnO occupies the lipophilic cavity, and 3,4-dichlorophenyl orients towards the lipophilic tunnel. Only binding site residues (stick, cyan) forming hydrogen bonds or  $\pi$ - $\pi$  interactions with ligand are displayed. Yellow dashed lines represent hydrogen bonds, and light blue dashed lines represent  $\pi$ - $\pi$  interactions. Molecular surface of ATX represented by transparent purple surface.

**Figure 7.** Two de-wetted cavity regions (blue, mesh) exist in the binding site. Only one of these sites is partially occupied by the crystal ligand (green, ball and stick) in 3WAX structure. Superposed IFD pose reveals that both of these sites are occupied by compound (*S*)-**25** (orange, ball and stick).  $Zn^{2+}$ -ions represented as spheres.

**Figure 8.** ATX-induced melanoma cell migration and its inhibition by compounds (*S*)-**25** and HA155. (a) Representative images of cell migration assay after 4 h incubation with medium, 150 nM LPA, 50 nM hATX + 50  $\mu$ M LPC or 50 nM hATX + 50  $\mu$ M LPC + 1  $\mu$ M (*S*)-**25**. Blue staining marks migrated cells and black circles represent the pores of the membrane. (b) The overall cell migration was stimulated with the addition of LPA or ATX + LPC, and was inhibited with the addition of ATX + LPC with compound (*S*)-**25** or HA155. Additionally, HA155 inhibited LPA-stimulated migration in a statistically significant manner. Values are mean + SEM from three independent experiments with duplicate chambers, each counted from eight different fields for Medium; Medium with 0.1% DMSO; 150 nM LPA and 0.1% DMSO  $\pm$  Inhibitors; and 50 nM hATX with 50  $\mu$ M LPC  $\pm$  Inhibitors. Statistical analysis was conducted with 1-way-ANOVA followed by Tukeys multiple comparisons between treatments. The level of significance is indicated with asterisk: NS, nonsignificant ( $p > 0.05$ ); \* $p \leq 0.05$ ; \*\* $p \leq 0.01$ ; \*\*\* $p \leq 0.001$ .

Graphical abstract